Summer 2020

Doping Effects on Transition-Metal Silicides: Crystal Structures and Physical Properties of Aluminium Doped Rhenium Silicide

Victoria DeCocq
Missouri State University, vic1003@live.missouristate.edu

DOPING EFFECTS ON TRANSITION-METAL SILICIDES: CRYSTAL STRUCTURES AND PHYSICAL PROPERTIES OF ALUMINIUM DOPED RHENIUM SILICIDE

A Master's Thesis

Presented to

The Graduate College of

Missouri State University

In Partial Fulfillment

Of the Requirements for the Degree

Master of Science, Chemistry

By

Victoria DeCocq

August 2020

DOPING EFFECTS ON TRANSITION-METAL SILICIDES: CRYSTAL STRUCTURES AND PHYSICAL PROPERTIES OF ALUMINIUM DOPED RHENIUM SILICIDE

Chemistry

Missouri State University, August 2020

Master of Science

Victoria DeCocq

ABSTRACT

Semiconductive transition-metal silicides (*e.g.,* ReSi) express weak thermoelectric properties. These properties can improve through n-type or p-type doping (*e.g.,* Al), resulting in altered crystal structures. Binary rhenium silicide ($ReSi_{1.75}$) exhibits promising thermoelectric properties and an intriguing crystal structure. Previous research has shown $ReSi_{1.75}$ changes from a commensurate supercell $MoSi_2$-type structure to an incommensurate superspace group structure, when doped with aluminium to $ReAl_{0.074}Si_{1.67}$. $ReSi_{1.75}$ expresses a figure of merit (ZT) of 0.70 at 800°C, which improves to a ZT of 0.95 at 150°C for $ReAl_{0.02}Si_{1.75}$. Because of the interesting properties expressed by rhenium silicide and the Al-doped variants, my research involves al-doping of rhenium silicides at various doping ratios, using the (18-n) electron rule, to determine how crystal structures and physical properties are affected. Using a non-thermal plasma arc furnace, (MRF SA200-1-VM), Al-doped rhenium silicides were synthesized. Half of the samples were annealed at 1000°C for a week, while the other half remained As Cast. Crystal structures and the bulk composition was determined using SXRD, PXRD and neutron diffraction, which was refined using Jana 2006. The resulting crystallographic data showed a transition from an incommensurate composite superspace group structure when Si-rich, to a *P4/nmm* space group for ReAlSi, and finally to a *I4/mmm* space group for the Al-rich samples. Neutron diffraction showed Al and Si were segregated with a 1:1 doping ratio but became mixed through increased Al-doping; these findings were substantiated using computational chemistry. Both ReAlSi and $ReAl_{1.2}Si_{0.8}$ became superconductive below 3.5K, with transition temperatures occurring above 4K. Though the resistivity, at temperatures above 3.5K, was ten-times higher for ReAlSi compared to $ReAl_{1.2}Si_{0.8}$.

KEYWORDS: crystal structures, physical properties, semiconductive transition-metal silicides, thermoelectric, doping, incommensurate, superconductive

DOPING EFFECTS ON TRANSITION-METAL SILICIDES: CRYSTAL STRUCTURES AND PHYSICAL PROPERTIES OF ALUMINIUM DOPED RHENIUM SILICIDE

By

Victoria DeCocq

A Master's Thesis
Submitted to the Graduate College
Of Missouri State University
In Partial Fulfillment of the Requirements
For the Degree of Master of Science, Chemistry

August 2020

Approved:

Fei Wang, Ph.D., Thesis Committee Chair

Gary Meints, Ph.D., Committee Member

Tiglet Besara, Ph.D., Committee Member

Eric Bosch, Ph.D., Committee Member

Julie Masterson, Ph.D., Dean of the Graduate College

ACKNOWLEDGEMENTS

Thank you to my collaborators without whom, this thesis would be brief. Specifically, thank you to Alec Neesen, for the computational contributions; Hillary Warden, for the single crystal data of the incommensurate crystals too complicated for our single crystal diffractometer; Dr. Weiwei Xie for the physical property data and analysis; and Dr. Thomas Heitmann for neutron diffractions.

I would like to thank the following people for their support during the course of my graduate studies. Megan Westwood, for the endless supply of Almond Hersey Kisses™ needed to write this thesis. Dr. Meints, for the consistent reassurance, and for all the gloves I borrowed from your research group that you don't know about. Dr. Bhattacharrya, for our publication and words of wisdom. Linda Allen because she is the rock of this department. To all my fellow graduate students because misery loves company.

Dr. Wang was the MVP in producing this thesis and research. His dedication in helping me understand our research was incalculable. He was extremely patient, kind and compassionate, frequently setting aside time to re-explain concepts I struggled with and sought out how to explain concepts in various ways to help me. He went above and beyond the call of duty as a research advisor and even acted as an emotional mentor for me when I became overwhelmed and felt defeated. I cannot express my gratitude enough towards Dr. Wang, 10/10 would recommend.

TABLE OF CONTENTS

LIST OF TABLES

LIST OF FIGURES

CHAPTER 1: INTRODUCTION

1.1 Crystallography

Crystal structures can help explain physical properties of a compound, such as the differences between graphite and diamonds, despite both being comprised solely of carbon atoms. Crystals are defined by long range order and structural anisotropy. [1] Crystallography determines the arrangement of atoms through diffraction patterns generated by bombarding the crystal with X-rays, electrons or neutrons. Since Al-doped rhenium silicides are promising thermoelectric candidates, their crystal structures and physical properties were determined through research presented in this thesis. To understand crystallographic data, there must be a basic understanding of crystal structures.

The three-dimensional arrangement of atoms within a crystal structure are described using a crystal lattice, which is comprised of unit cells. Edges of the unit cell lie along three non-coplanar vectors (x, y, z) and are denoted as (a, b, c) with the angles between the edges given as α, β, and γ. Unit cells are described by these six lattice parameters: a, b, c, α, β, and γ. There are three rules for determining the correct unit cell: [1]

1. The symmetry of the unit cell should be identical to the symmetry of the lattice with the exception of translational symmetry.
2. The unit cell must meet the parameters of the seven crystal systems.
3. The smallest volume unit, or one with the least number of lattice points, is desirable.

Crystal systems comprise the gross classification of crystal structures. [2] The geometric bases of crystals are the Bravais lattice, which are distributed among the seven crystal systems, of which there are fourteen Bravais lattice unit cells determined to be compatible with the orderly arrangement of atoms found in crystals. [2] Table 1 depicts the Bravais lattices, the vacancies in the table are due to limitations by the unit cell rules. For example, centered triclinic

unit cells can simply be made primitive and thus yield a smaller volume unit cell, which corresponds to rule number three. The diversity in lattice structures arises from various symmetry elements and respective orientations. [1] Traditional crystal structures can be described with space groups (of which there are 230) whose members include rotational (*e.g.,* rotation about an axis, reflection in a plane, inversion about the center) and translational symmetry operations. [2]

Table 1. Bravais lattices.

Crystal system	Unit Cell Symbol/s	Axial relationships in conventional unit cell	Symmetry at each lattice point
Triclinic	*P*	a≠b≠c α≠β≠γ≠90°, 120°	$\bar{1}$
Monoclinic	*P, C*	a≠b≠c α≠β≠γ≠90°, 120°	2/*m*
Orthorhombic	*P, C, I, F*	a≠b≠c α=β=γ=90°	*mmm*
Tetragonal	*P, I*	a=b≠c α=β=γ=90°	4/*mmm*
Trigonal (Hexagonal axes)	*P*	a=b≠c α=β=90° γ=120°	$\bar{3}$*m*
Trigonal (Rhombohedral axes)	*R*	a=b=c α=β=γ≠90°,<120°	$\bar{3}$*m*
Cubic	*P, I, F*	a=b=c α=β=γ=90°	*m*3*m*
Hexagonal	*P*	a=b≠c α=β=90° γ=120°	6/*mmm*

Modified from Ref. 2. [2]

With the Bravais lattice acting as a framework for the crystal structure, the atoms in crystals can either sit on the points of the lattice or sit in some fixed relation to these points. This means that the atoms within the crystal structure will arrange with periodicity and this arrangement will express many of the same symmetry operations as the lattice. [3] Additional rules are necessary when the crystal structure contains compounds, and these rules are:

1. "Body-, face-, or base centering translations, if present, must begin and end on atoms of the same kind." [3]
2. Each set of similar atoms must separately possess the same symmetry elements as the crystal structure; such that when a symmetry operation is performed one atom will give coincidence to an atom of the same type. [3]

The first rule is demonstrated in Figure 1 where the unit cell shows that atoms of the same type comprise the same positions on the lattice. The second rule can be envisioned using the unit cell in Figure 1, where if a 90° rotation about any axis were to occur a chlorine atom would replace a chlorine atom and vice versa for sodium. [4]

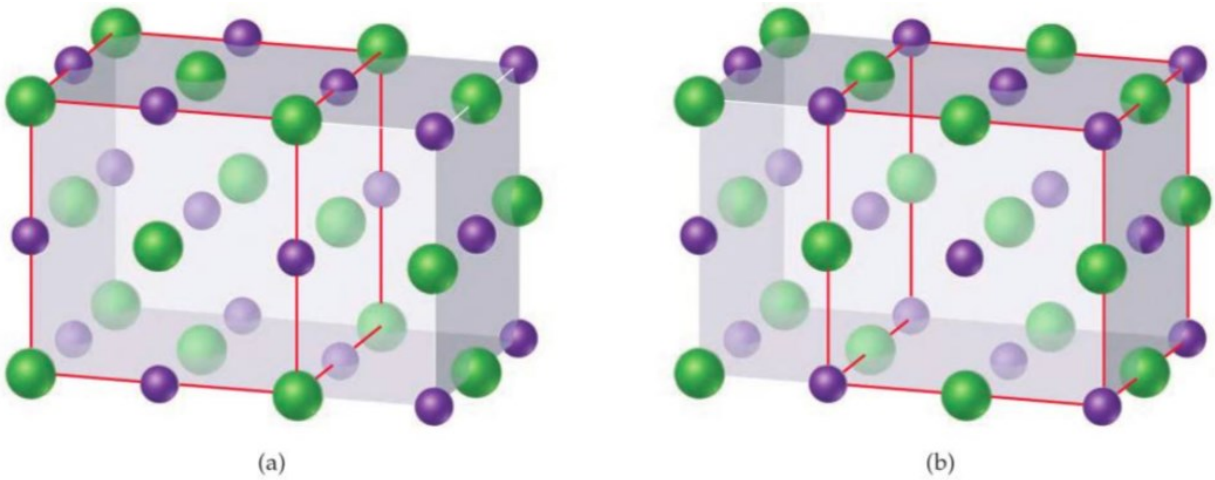

Figure 1. Defining a crystal lattice. The purple spheres depict sodium, while the green spheres represent chlorine, outlined in red are different but equally valid unit cells. (a) The atoms of chlorine on the corners and face, and sodium on the edge and center this is shifted in (b) showing rule 2. Reprinted from Ref. 4. [4]

Atoms sitting on the face, edge, or corner of a lattice will occupy only a fraction of the unit cell, such that a body-centered cubic structure will essentially have a multiple of two atoms per unit cell (shown in Figure 2). [4] This information yields insight into how atoms stack and the density of a unit cell. In addition, the types of atoms in a compound have an effect in determining the Bravais lattice of the crystal structure. For example, CsCl and NaCl are both ionic compounds, belonging to the cubic crystal system, but the structure for CsCl is body-centered, while NaCl is face-centered due to the difference in atomic radii of Cs compared to Na, thus effecting how the atoms stack. [3]

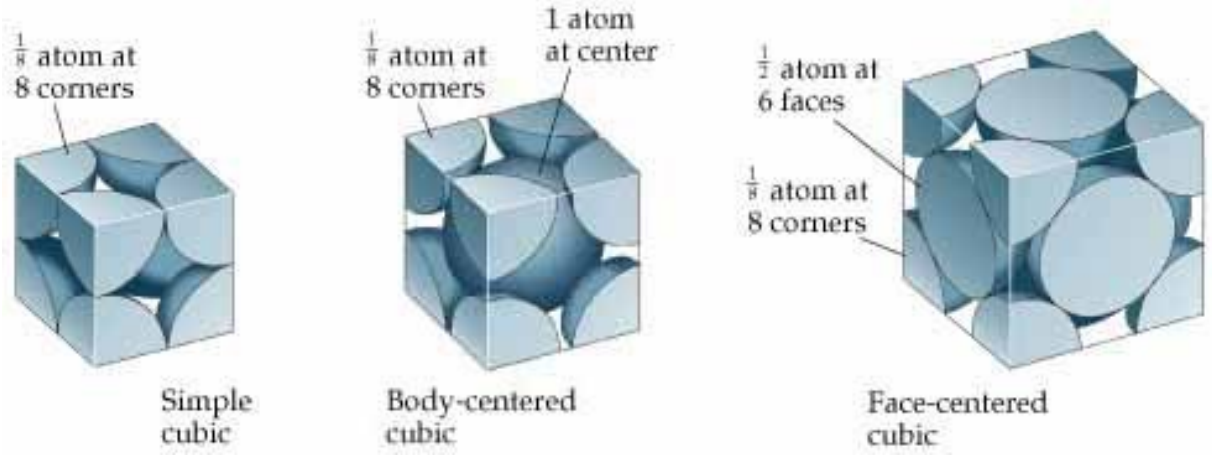

Figure 2. Space filling model. This is a depiction of how atoms can fill various unit cells. Reprinted from Ref. 4. [4]

Miller indices, (*hkl*), are used to indicate a set of parallel planes within a crystal structure and are determined by crystallographic axes through the reciprocal of the intersection of the plane with the axes (Figure 3). [5] Due to being reciprocal, when a plane intersects the unit cell at half-length, the Miller index is 2, and when the intersection occurs infinitely the value is denoted as 0. The distance between neighboring planes is known as d-spacing and is used in Bragg's law (mentioned in depth when discussing X-ray diffraction). [1]

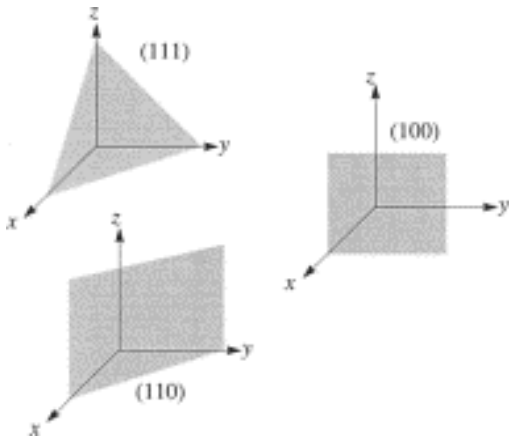

Figure 3. Miller indices. This is a pictorial representation of a few Miller indices possible for a unit cell. Reprinted from Ref. 5. [5]

1.1.1 X-ray Diffraction. Radiation of a wavelength around the same order of magnitude as the crystal's lattice spacings will generate a diffraction pattern of the crystal in reciprocal space. [6] Lattice spacings are determined by the distances between atoms (or chemical bond lengths), typically ~0.8 to 3.0 Å, which is comparable to the wavelength of X-rays ~0.5 to 2.5 Å.[7] Bragg's law provides the conditions necessary for diffracted X-ray waves to result in constructive interference from a family of lattice planes. [8] Bragg's law states that $n\lambda=2d\sin(\theta)$ where n is an integer (the order of reflection), λ is the X-ray wavelength, d is the distance between the crystallographic planes of the lattice, and θ is the angle of the incident beam of X-rays with respect to the crystallographic planes (shown in Figure 4). [9]

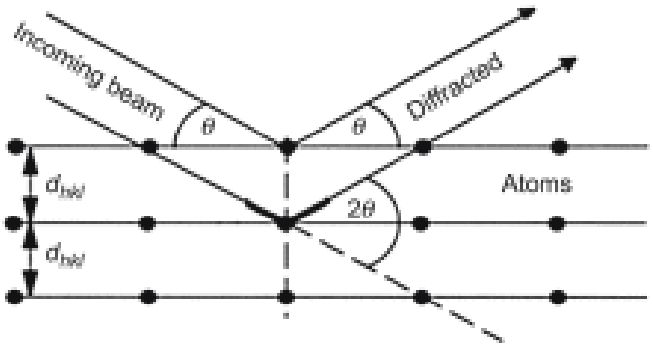

Figure 4. Bragg's law. This image shows a constructive interference diffraction wave, which will generate a diffraction peak explained by Bragg's law. Reprinted from Ref. 9. [9]

The refraction index for X-rays is approximately one; therefore, the diffracted X-rays cannot be focused with lenses to produce an image of the crystal structure directly. [1] Instead, diffraction patterns are used to construct a reciprocal lattice of the crystal structure in reciprocal space, which has the same symmetry as the crystal lattice in real space and therefore can be transformed into real space. [1] The crystal structure can then be solved and refined with mathematical methods (*e.g.,* charge flipping) based on the reciprocal lattice and the intensities of diffracted X-rays.

Cathode ray tubes are used to generate X-ray radiation through the excitation and relaxation of electrons in an anode element. The wavelength of the radiation emitted depends on the anode element and the atomic shells the electrons are "jumping" between. The innermost atomic shell, depicting ground state, is denoted as K, which is encompassed by atomic shell L and then shell M; these correspond to the principal quantum number $\boldsymbol{n}$= 1 ,2, 3... [3] When an excited electron from shell L returns to K, Kα radiation is emitted; whereas Kβ radiation is emitted when the electron returns to K from the M atomic shell. Kα radiation is about five times more intense than Kβ since vacancies in shell K are more likely to be filled by electrons from closer atomic shell L. [3] Diffraction clarity requires monochromatic X-rays, therefore, filters and monochromators are used to remove the less intense Kβ radiation. Powder X-ray diffraction (XRD) usually employs copper as the anode material to generate its characteristic (Kα) X-ray, with a wavelength of 1.54433 Å. Molybdenum has a Kα of 0.71354 Å and is usually used for single crystal XRD anode material. [7] The X-rays are collimated and directed towards the sample at various angles. The sample rotates in the beam at an angle of θ, while a detector revolves around the sample at an angle of 2θ. A goniometer is used to maintain the angle of the incident beam and the rotation of the sample. The detector, usually a charge coupling device, detects X-

ray photons from the diffracted X-rays, which are converted to visible light by a phosphor (usually Tb^{3+} doped with Gd_2O_2S). [1] Phosphor is a substance that luminesces under excitation.

Simple crystal structures could be easily solved with single-crystal XRD (SXRD), which yields full crystallographic information, such as the space groups, the dimensions of the unit cells, bond lengths as well as angles, and the ordering of the sites. However, due to the sample requirements, there are limitations for SXRD. The samples must be small single crystals whose sizes are tens to hundreds of micrometers. Such small crystals may not represent the bulk of the material it is taken from, especially when the material is a mixture of two or more phases. In addition, single crystals are not always found for a material. In comparison, it is much more challenging to solve crystal structures from scratch using powder XRD (PXRD). However, PXRD analyzes bulk samples, enabling analysis of multiple crystalline phases coexisting in a sample through whole-pattern refinement. The difference in diffraction patterns generated by SXRD and PXRD are shown in Figure 5. [10]

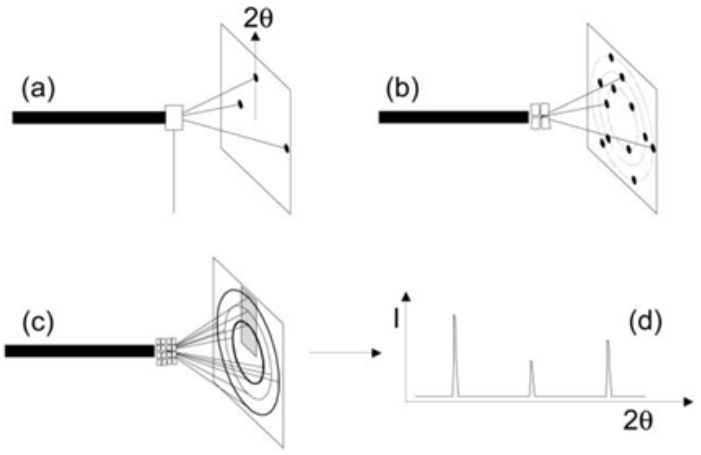

Figure 5. Pictorial representation of SXRD and PXRD generation. (a) Shows diffraction from a single crystal, (b) is diffractions from four domains within the crystal, (c) is a powder sample generating Debye rings, which when cross-sectioned show a spectra (d). Reprinted from Ref. 10. [10]

Neutron diffraction differs from SXRD and PXRD because “neutrons are scattered on the

nuclei " of the atoms instead of electrons. [1] Neutron diffraction is advantageous due to the ability to differentiate between elements close to each other on the periodic table, which is not possible using X-ray diffraction. X-ray diffraction relies on electron density (electron count) to analyze the crystal structure. Elements close to each other on the periodic table vary in electron count by 1 and since electrons are smaller than neutrons X-ray diffraction cannot differentiate between two similar electron count elements.

1.1.2 Incommensurate Structures and Superspace Group. Any material with a discrete diffraction pattern constitutes a crystal even if three-dimensional lattice periodicity is lost. [11] A subcategory of aperiodic crystals are incommensurate crystals, which express an incommensurable relationship between two or more sets of periodicities within the same crystal. Incommensurate crystals include incommensurate modulated crystals, incommensurate magnetic structures and incommensurate composite crystals. [11] For modulated crystals, a wave vector (**q**) quantifies the amount of modulation expressed in the periodicity of a crystal through a ratio between the average structure unit cell dimensions and the wavelength of the modulation. [12] A rational wave vector denotes a commensurate crystal structure, which can be equivalently described using a supercell structure of the average structure. [12] The supercell structure essentially expands the average structure's unit cell until it accounts for the modulation. Incommensurate modulated structures have an irrational wave vector. [11] A comparison between commensurate and incommensurate modulated structures can be seen in Figure 6. The real space atoms, in the incommensurate structure are skewed by an irrational wave vector and therefore cannot be described with a super cell structure. The skewed position of atoms, in the incommensurate structure, is emphasized using red and blue arrows. Incommensurate magnetic structures have a periodic crystal structure, but the ordered magnetic moments are

incommensurate with the periodicity of the crystal structure and can only be determined through neutron diffraction. Incommensurate composite crystals are comprised of two sublattices in the same crystal whose lattice parameters are incommensurate with each other. [11]

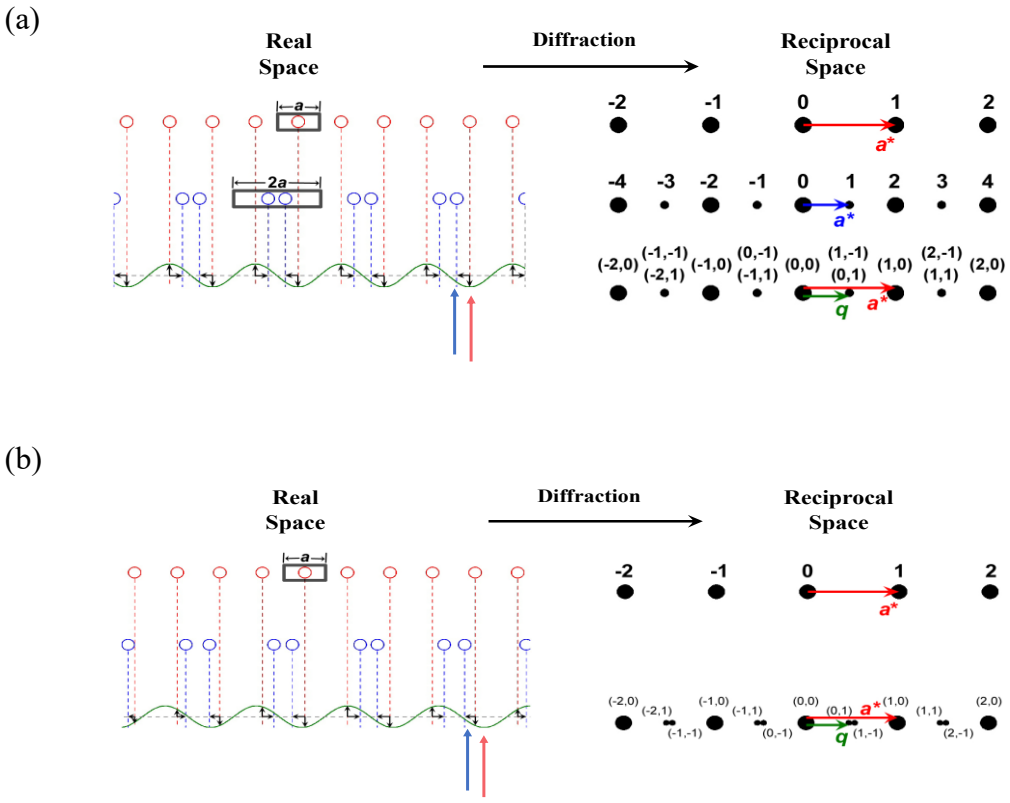

Figure 6. Commensurate versus incommensurate structures. (a) Shows commensurate modulation, while (b) depicts incommensurate modulation.

Incommensurate crystallography requires determination of the shapes and amplitudes of the modulation wave, and the crystal structures must be described using superspace groups. [12] The Dictionary of Crystallography defines superspace group as:

> An (m+d)-dimensional *superspace group* is an n-dimensional space group (with n=m+d) such that its point group leaves an m-dimensional (real) subspace (m=1,2,3) invariant. An aperiodic crystal structure in m-dimensional physical space may be obtained as the intersection of the m-dimensional subspace with a lattice periodic structure in the n-dimensional space. [13]

1.2 Semiconductivity

The energy bands (valence and conduction) are formed in crystalline structures because the discrete energy levels of atoms spread through atomic interactions. [14] Electrical conductivity is determined by both the size of the band gap (which lies between the valence and conduction band) and the electronic states. The conductivity is categorized as either a conductor, insulator or semiconductor. Conductors have a conduction band that overlaps with the valence band, therefore the flow of electrons between the states is continuous, while the band gap is too large for insulators and thus the flow of electrons is inhibited (Figure 7). At absolute zero, all the electrons in a semiconductor occupy the valence band. As temperatures increase, thermal oscillation of the crystal lattice provides a source of energy, and when this energy is at least equal to the energy band gap, electrons are excited into the conduction band leaving behind a hole. Both the excited electrons and vacancies contribute to the conductivity of the material, known as n-type conductivity and p-type conductivity, respectively. [15] Technological advancement relies heavily on semiconductive material, with silicon being the most common element in semiconductors, comprising 95% of semiconductive materials sold world-wide. [14] Utilized for power efficiency, reliability and reasonable prices, semiconductive material is used in signal processing, computation and control applications.

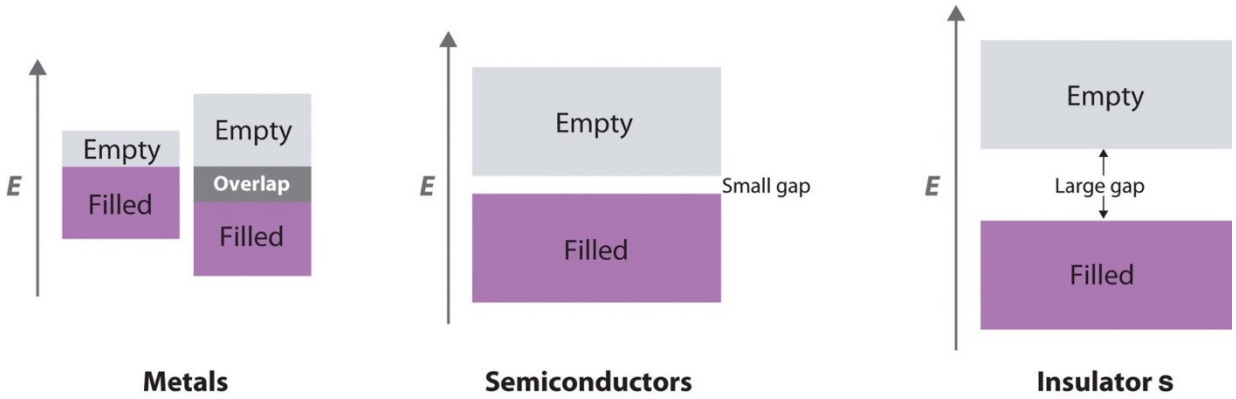

Figure 7. Conductivity of metals, semiconductors and insulators. Reprinted from Ref. 16. [16]

Doping of semiconductors with impurities has been shown to improve conductivity in one of two ways (Figure 8). N-type doping occurs when the impurities contain more valence electrons than the host lattice, thus providing electrons to the conduction band, at lower temperatures than originally necessary, with a disproportionate number of holes generated in the valence band. [15] The holes generated in the valence band, through p-type doping, enable the flow of electricity by lowering the acceptor level of the conduction band. The ability to control the amount of conductivity a semiconductor expresses offers diversity and makes semiconductive material highly versatile. Simply doping 10 boron atoms into a system of a million silicon atoms would result in improved electrical conductivity by a thousand-fold. [14] The doping of intrinsically semiconductive elements, such as silicon, is used in a plethora of materials. Transistors, enabling the binary system for computers, is sandwiched p-type and n-type semiconductors with a second circuit added to the system to act as a switch.

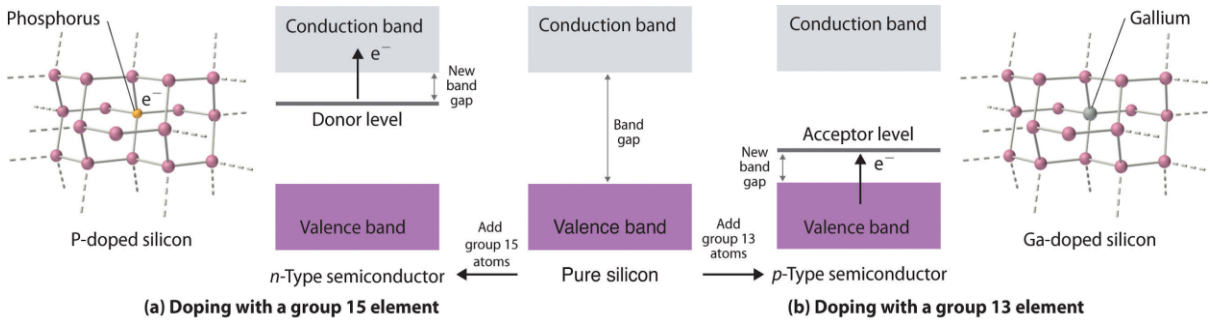

Figure 8. Doping of semiconductors. (a) N-type doping and (b) P-type doping lower the band gap energy. Reprinted from Ref. 16. [16]

1.3 Thermoelectricity

Thermoelectricity is the ability for a material to convert heat into electricity and vice versa, and is a phenomenon expressed by semiconductors. [17] This physical property can be

described by the Seebeck effect, Peltier effect and Thompson effect, which are all inter-related. The Seebeck effect describes the generation of a potential difference from the temperature difference between two dissimilar conductive materials. An electric current passing through a junction connecting the dissimilar materials causing the release or absorption of heat is described by the Peltier effect. The Thompson effect describes a current flowing through a conductor with a temperature gradient, along the current direction, causing the release or absorption of heat. [17] Heavily doped semiconductors make great thermoelectric material due to an excess of free electrons or "holes", depending on the type of doping. A temperature difference is used to induce charge-carrier flow within semiconductors, and this property can be manipulated through effective mass, degeneracy, and band gap to engineer the electronic band structure. [18] The Seebeck coefficient is used to quantify the quality of the thermoelectric material and received its name from the Seebeck effect. [17] The Seebeck coefficient is calculated as the change in voltage over the change in temperature. The dimensionless figure of merit ($zT = T\frac{S^2\sigma}{k}$) quantifies the efficiency of converting heat to energy, where S is the Seebeck coefficient, σ represents the electrical conductivity, k is the thermal conductivity of the thermoelectric material and T is the absolute temperature. [17] The mathematics calculating the figure of merit shows a high electrical conductivity with a low thermal conductivity is desired in order to increase the figure of merit. A low thermal conductivity and high electrical conductivity are, however, conflicting (*e.g.,* a good electrical conductor, such as metal, usually has high thermal conductivity, too). The conflicting nature of thermal conductivity and electrical conductivity can be manipulated in semiconductors and thus optimized, this is seen in Figure 9. Intrinsic defects and doping are ways to compensate for the conflicting nature of low thermal conductivity and high electrical conductivity, in order to optimize thermoelectricity.

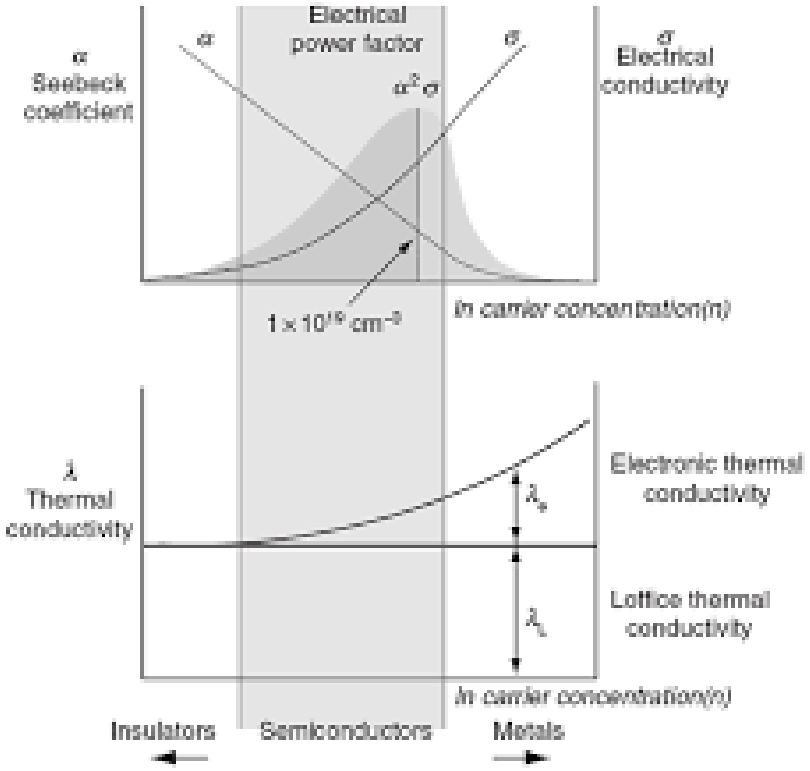

Figure 9. Optimization of thermoelectricity. Reprint from Ref. 19. [19]

Thermoelectricity is generated through a temperature gradient between two dissimilar metals. A potential difference is generated between hot and cold end due to charge carriers flowing within a solid along with heat. [19] Heat is, therefore, utilized in thermoelectric material to produce energy. According to the Lawrence Livermore National Laboratory (LLNL) nearly two thirds of energy produced is lost as heat waste. [20] Utilization of this technology could improve the overall efficiency of energy use in the US, thus lowering, not only carbon emissions but dependency on foreign sources. This material is also desirable to NASA in regard to space travel due to "their reliability, absence of moving parts, and silent operation" despite the high cost and low efficiency. [19] Thermoelectric material research has vast applicability and is focused on manufacturing large quantities of materials with a high figure of merit.

1.4 Superconductivity

The Encyclopedia of Britannica states that at a specific low temperature, known as the transition temperature (T_c), a superconductor is capable of transporting electrons with no resistance. This enables circulation of electricity without loss of energy, thus generating zero heat waste. In 1957 three American researchers, John Bardeen, Leon Cooper, and John Schrieffer, established the theory of superconductivity known as the BCS theory. This theory states that Cooper pairs (electrons which pair through lattice vibrations) move around the crystal structure without friction, and they function as a single entity with opposite spins (bosons). When an electrical current is applied to a superconductor the Cooper pairs move through the crystal lattice, thus producing a current, which continues to flow even after the voltage is removed due to Newton's first law of motion. [21] This is caused by the lattice structure being composed of positive ions surrounded by a cloud of electrons and as the electrons move through the structure, the positive ions feel an attractive force causing a slight movement of the structure, or a distortion of the lattice. A positive feedback loop is generated due to this movement attracting another electron thus producing a Cooper pair. These electrons are weakly paired and easily disrupted by thermal energy, thus the need for low temperatures. [22]

Superconductors express a phenomenon known as the Meissner effect, in which the material produces a weak, external magnetic field on its surface. This is caused by the expulsion of the magnetic field because superconductors are perfectly diamagnetic. The expulsion of the magnetic field enables levitation. Superconductors do not expel the magnetic flux entirely, there is an electromagnetic penetration depth at which a magnetic field will be present, and this depth increases with increasing temperature until the transition temperature is reached. An applied magnetic field can also break apart the Cooper pair, by suppressing the Meissner effect thus

converting the superconductor back to a normal state much like increasing the temperature above the transition temperature does. The minimum amount of an applied magnetic field required to break the Cooper pair is known as the critical field. [22] This type of material is utilized in many industrial processes including magnetic levitation trains, MRI's and Nuclear Magnetic Resonance instrumentation.

1.5 Rhenium Silicide

The vast utility of semiconductors encourages research into transition-metal silicides. Intrinsically semiconductive, silicon has a band gap of 1.12 eV, falling within the industrially desired range of 0.5 to 2.5 eV. [14] The transition-metal silicide $ReSi_2$ was reported to have an energy band gap of 0.2 eV, measured using electrical resistivity and optical reflectivity. [23] Computational research, by Qui *et al*., involving binary rhenium silicide, substantiated this claim "using the full-potential linearized augmented plane-wave method in the local density approximation with self-interaction correction and the semiclassical Boltzmann theory". This group was able to determine the indirect gap for $ReSi_{1.75}$ was 0.12 eV and the direct gap was 0.36 eV. [24] The research also showed that, when doped with Al, the Fermi levels did move into the valence band, and the compound remained a semiconductor. In addition, the calculations suggested the Al-doped compounds were promising thermoelectric candidates with an orientation along the [100] direction. [24] Inui *et al*. has experimentally proven $ReSi_{1.75}$ is thermoelectric with a figure of merit (ZT) of 0.7 at 800K. Through doping with 2 at. -% of Al, the ZT value improved to 0.95 at 423K, nearing the ZT necessary for commercialization, which is greater than one. The improved thermoelectric properties are likely due to an increase in positive density within the crystal structure, allowing less electrical resistivity. [25]

The complicated crystal structure of $ReSi_{1.75}$ was argued to have *I4/mmm*, *Immm*, *P1*,[26] and most recently a *Cm* space group. [25] Three articles agreed $ReSi_{1.75}$ has a commensurate $MoSi_2$-type superstructure with ordered Si vacancies, shown in Figure 10. Orange boxes highlight the section of vacancies, in Figure 10, which result from the removal of orange Si/Al atoms with the light blue Si/Al atoms accommodating the space. The position of the Si vacancies varied in each report, though the vacancies stay as far from one another as possible. [27] Al-doping resulted in incommensurate crystals structures, with $ReAl_{0.1}Si_{1.675}$ exhibiting an orthorhombic superspace group structure of *X2mm(a00)s0s*, though still a $MoSi_2$-type basic structure with different Si vacancy positions, shown in Figure 10. [28] The structural complexity could contribute to the improved physical properties and therefore more insight into these structures and their respective properties is desirable.

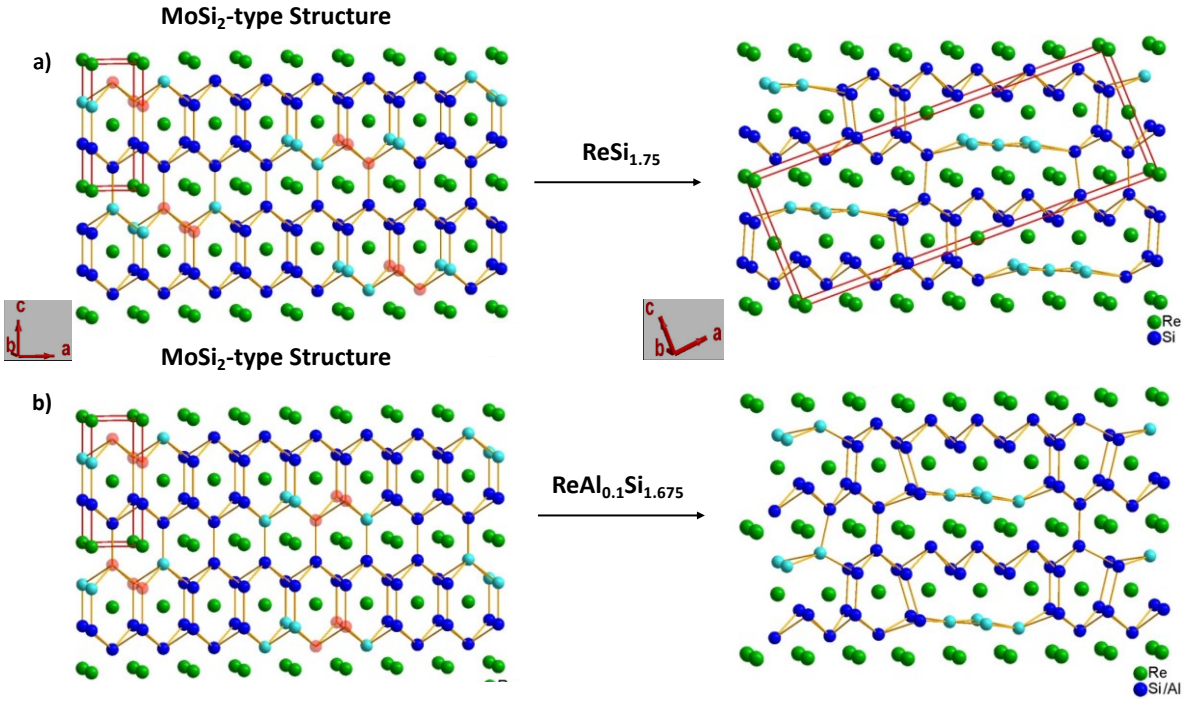

Figure 10. $MoSi_2$-type structure variations in $ReSi_{1.75}$ and $ReAl_{0.1}Si_{1.675}$. a) Shows the variations made from the $MoSi_2$-type structure to the actual $ReSi_{1.75}$ structure. b) Shows how the $MoSi_2$-type structure varies from the Al-doped crystal structure. Adapted from Ref. 27. [27]

In addition to expressing semiconductive and thermoelectric properties, Al-doped rhenium silicides are promising superconductive candidates. Through doping, some semiconductors, which otherwise would not have a T_c (*e.g.*, SnTe), are able to enter a superconductive state. [22] At low temperatures, hundreds of known elements are able to become superconducting, including elemental Re and Al. [22] Al-Si alloys, reportedly, become superconductivity at 6.2 K. [29] Re-Si express superconductivity in quenched solid solution (Si ≈ 10 %atom, T_c = 5.2 K), [30] and compounds of both Re_2Si and ReSi express superconductivity at T_c = 3.8 K, [31] and T_c = 1.7 K [23] respectively. These previous reports show that Al-Si and Re-Si compounds can express superconductivity, therefore it is feasible to predict an Al-doped ReSi compound could become superconductive at a specific low temperature. Research regarding the superconductive nature of rhenium-poor ($ReSi_{1.75}$) or Al-doped rhenium silicides have yet to be reported.

1.6 (18-n) Electron Rule

A factor of the structural diversity of intermetallic compounds is the electron count. [32] Intermetallics are comprised of transition metals (T) and main group elements (E). Transition metals require (18-n) electrons in order to obtain a closed-shell electron count, where the n is equal to the number of homo-atomic bonds. [33] Using reversed approximation molecular orbital (raMO) analysis, the sp3 bonding functions are directed along T-T contacts, in which each bond covalently shares the electron pair thus contributing to the electron count. The electron count for transition metals in group 9 (*e.g.,* Re) is 14 valence electrons per formula unit (f.u.) due to the formation of four isolobal bonds shared between transition metals. [34] The structural complexity of $ReSi_{1.75}$ and Si vacancies are governed by the (18 – n) electron rule. [35] In the crystal structure

of $ReSi_{1.75}$ and $MoSi_2$ n=4, thus requiring fourteen valence electrons per formula unit (f.u.) ($ReSi_{1.75}$: $7 + 4 \times 1.75 = 14$) and ($MoSi_2$: $6 + 4 \times 2 = 14$). Therefore, vacancies are necessary for binary rhenium silicide to obtain a closed-shell electron count. This rule was used to determine the doping ratio of silicon and aluminium, as shown in Table 2.

Table 2. (18-n) electron rule.

$ReAl_XSi_Y$=14 valence electrons								
X	0.200	0.300	0.400	0.500	0.600	0.700	0.800	0.900
Y	1.600	1.525	1.450	1.375	1.300	1.225	1.150	1.075

CHAPTER 2: EXPERIMENTAL DESIGN

2.1 Synthesis

The various doping ratios of ReAlSi were synthesized using a non-thermal plasma arc furnace (MRF SA200-1-VM), in a vacuum chamber of argon gas to prevent oxidation. The samples were prepared using Re foil (Alfa Aesar, 99.97%), Si rod (Alfa Aesar, 99.999%), and Al wire (Alfa Aesar Puratronic, 99.999%). The amount of Al doped with ReSi was calculated using (18-4) electron rule for the silicon rich series (Table 2). There was an inverse variation in ratio of 0.1 between Al and Si in the Al-rich series. Each sample was rotated and melted at least three times, then divided into two portions, one as-cast and the other annealed. The annealing took place in a box furnace set at 1000°C for a week.

2.2 Analysis

2.2.1 Crystallography. Each sample was analyzed using single crystal X-ray diffraction (SXRD) and powder X-ray diffraction (PXRD). PXRD sample analysis was collected at room temperature using a Bruker D8 Discover diffractometer with a monochromatic Cu anode ($K\alpha_1$ = 1.5406, $K\alpha_2$ = 1.54439) and an area detector. The 2θ range was set at 15 – 90°, with a step size of 0.02, and an exposure time of 1 second per step. The SXRD collected at room temperature using a Bruker APEX I with a CCD detector and a Mo radiation source (λ = 0.71073 Å). The Bruker SMART package was used to correct for absorption and for data reduction.

Neutron diffraction (ND) was necessary to distinguish aluminium atoms from silicon atoms. This was done on the PSD diffractometer located at University of Missouri Research Reactor. The neutron wavelength used was 1.486 Å with a scan step width of 0.05° and an angle

range from $4.45° \leq 2\theta \leq 104.4°$. The neutrons were counted using a set of five linear position detectors.

All diffraction patterns were refined using Jana 2006 crystallographic computing software, capable of determining/refining structures from X-ray and neutron diffraction data.[36]

2.2.2 Computational. Vienna Ab Initio Software Package (VASP) was used to determine the distribution of Al and Si atoms through first-principle calculations. [37] Pseudopotentials, for Re, Al, and Si, were generated with projector augmented-wave (PAW) method. The electronic exchange correlation was treated with the Perdew-Burke-Ernzerhof (PBE) generalized gradient approximation. [37] The energy cut-off of the plane wave basis functions was 306.7 eV. A 9 × 9 × 5 Monkhorst mesh was used to sample the 1st Brillouin zones of the single cell model structures, which was adjusted for the supercell model structures. The Brillouin zone is a Wigner-Seitz primitive cell in the reciprocal lattice. These model structures were optimized using the conjugate gradient algorithm with fixed unit cell volumes. The chemical bonding of various, computational models of the structures was analyzed by calculating their respective integrated crystal Hamilton populations (ICOHP's) with the LOBSTER program. [37]

2.2.3 Physical Properties. Quantum Design Dynacool physical property measurement system (PPMS) was used to determine temperature dependent magnetic susceptibility, resistivity and specific heat measurements of selected samples, ReAlSi and $ReAl_{1.2}Si_{0.8}$, whose arc-melted pellets were cut into flat discs which are 1 – 2 mm thick and ~ 0.5 mm in diameter with a diamond saw for measurements. Susceptibility was determined using both field cooling and zero field cooling methods. The standard relaxation method was used to determine heat capacity. The Ginsberg-Landau relation was used to determine the upper critical field limit, and the critical

temperature for our superconductive material. This relation is given as: $\mu_0 H_{c2}(T) = \mu_0 H_{c2}(0) \frac{(1-t^2)}{(1+t^2)}$, where $t = T/T_c$ and T_c is a fitting parameter (transition temperature at zero magnetic field). Heat capacity fitting results were calculated using: $C_p/T = \gamma + \beta T^2$, where γ and β are attributed to the electronic and lattice contributions to the heat capacity, respectively.

CHAPTER 3: SILICON-RICH RHENIUM-ALUMINIUM-SILICON TERNARY COMPOUNDS

3.1 Overview

Si-rich series include $ReAl_{0.2}Si_{1.6}$ up to $ReAl_{0.9}Si_{1.075}$. Si/Al vacancies are expected in this series, which can lead to incommensurate structures. The promising thermoelectric properties of $ReSi_{1.75}$ has caused several inorganic research groups to investigate the complicated crystal structure of this compound. Since it has been reported, by Inui *et al.*, that low-level Al-doping of $ReSi_{1.75}$ results in improved thermoelectric properties, which is closely related to the incommensurate structures, we decided to increase the doping ratio to investigate what affects that has on the crystal structure.

$ReSi_{1.75}$ has been reported to be a commensurate variant of the $MoSi_2$-type structure with a **q** vector of $\mathbf{q} = 1/8\mathbf{a^*} + 1/8\mathbf{c^*}$, where **a*** and **c*** are reciprocal lattice parameters. Our research supports previous claims that this modulation becomes incommensurate when aluminum is doped into the structure. So far, $ReAl_{0.1}Si_{1.675}$ is the only crystal structure that has been reported, and was reported as *X2mm(α00)s0s* with $\mathbf{q} = 0.1201\mathbf{a^*}$. [29] Since the **q** vector is irrational for the Al-doped variant the crystal structure is thus denoted as incommensurate, with incommensurate structures addressed in Chapter 1. Al-doping was done following the (18 – 4) electron rule, as discussed at the end of Chapter 1, and these samples were synthesized as described in Chapter 2. A few single crystals were selected from the samples and their crystal structures were determined using SXRD. These crystal structures confirmed our hypothesis that increased Al-doping would result in incommensurate crystal structures. The bulk compositions of the samples were determined using PXRD with interesting results.

3.2 SXRD

Among the single crystals that we selected from the Si-rich series of compounds, we identified 2 new incommensurate structures which have not been reported so far. The details of refinements are listed in Table 3.

Table 3. SXRD refinement information of the two new incommensurate crystal structures.

Loading Composition	$ReAl_{0.2}Si_{1.60}$	$ReAl_{0.4}Si_{1.45}$*
Crystal System, Space Group	Monoclinic, $X2/m(\alpha 0\gamma)00$[a]	Monoclinic $Pm(\alpha 0\gamma)0$[a]
Temperature (K)	293	293
Wavevectors	$\boldsymbol{q} = 0.1106\boldsymbol{a}^* - 0.0758\boldsymbol{c}^*$	$\boldsymbol{q} = 0.3266\boldsymbol{a}^* + 0.1928\boldsymbol{c}^*$
a, b, c (Å)	3.131(4), 3.148(3), 7.733(3)	7.748(2), 3.148(4), 3.148(4)
β (°)	90.05 (6)	90
Z	2	2
No. of measured, independent and observed [$I > 3\sigma(I)$] reflections	2980, 857, 423	5162, 3131, 1027
R_{int}	0.030	0.022
$(\sin\theta/\lambda)_{max}$ (Å^{-1})	0.648	0.771
R[$F^2 > 2\sigma(F^2)$], wR(F^2), S	0.031, 0.043, 1.18	0.029, 0.051, 1.20
Main R[$F^2 > 2\sigma(F^2)$], wR(F^2)	0.019, 0.027	0.025, 0.046
1st R[$F^2 > 2\sigma(F^2)$], wR(F^2)	0.065, 0.094	0.083, 0.137
2nd R[$F^2 > 2\sigma(F^2)$], wR(F^2)	0.069, 0.140	0.094, 0.146
3rd R[$F^2 > 2\sigma(F^2)$], wR(F^2)	0.085, 0.146	-
4th R[$F^2 > 2\sigma(F^2)$], wR(F^2)	0.130, 0.223	-
No. of reflections	857	3131
No. of parameters	77	144
No. of restraints	0	0
$\Delta\rho_{max}$, $\Delta\rho_{min}$ (e Å^{-3})	3.88, −5.50	4.36, −5.45

* The refinement is not 100% finished yet. The refined structure still includes some Si-Si distances that are too short. Further work is being conducted.

The diffraction patterns in the (*h*1*l*) reciprocal planes of two new incommensurate phases are shown in Figure 11. For both structures, the main reflections results in the same $MoSi_2$-type structure. When the satellite peaks are taken into account in refinement, the 2 structures, in Figure 11, both show Si/Al vacancies which are similar to those in $ReSi_{1.75}$ and $ReAl_{0.1}Si_{1.675}$ (Figure 10). However, the amount and the arrangement of the vacancies is different among these structures. For instance, vacancies occur every other Si/Al layer in the second new structure (Figure 11b) while in all the other structures, vacancies occur in every layer of Si/Al atoms. Si/Al vacancy accommodations are depicted using light blue atoms in Figure 11.

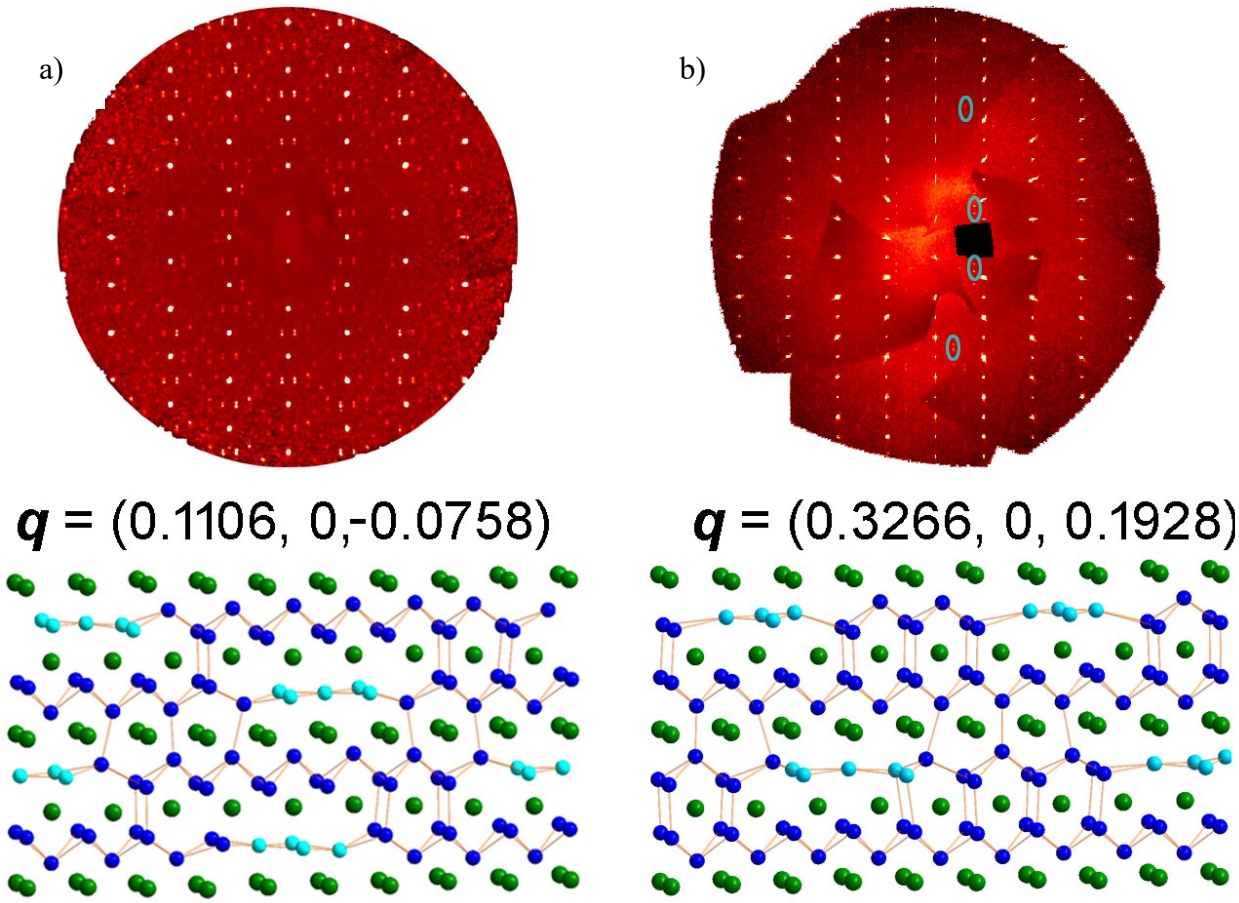

Figure 11. Incommensurate crystal structures. The (*h*1*l*) precession images, **q**-vector and crystal structure of (a) $ReAl_{0.2}Si_{1.6}$ and (b) $ReAl_{0.4}Si_{1.45}$.

These two new incommensurate structures further prove that we can subtly tune the crystal structures of rhenium silicides by doping with different amounts of Al atoms. The new phases may also possess desirable thermoelectric properties and are worth of testing.

3.3 PXRD

The PXRD data was refined using the results generated from the SXRD data. Since all of the incommensurate phases, the *X2/m(a0g)00*, *X2mm(a00)s0s*, and the *Pm(a0g)0*, all have the same $MoSi_2$-type average structure, their main reflections (strong peaks) are the same and can be indexed using the *Immm* space group. The PXRD refinement patterns for four different Si-rich samples are shown in Figure 12, with the remaining samples of the series in Appendix A. The powder diffraction data of the Si-rich samples showed multiphase compositions. As shown in Figure 12, samples with small amounts of Al-doping (*e.g.*, $ReAl_{0.3}Si_{1.525}$) were predominantly comprised of the phase that can be indexed with the *Immm* space group, with a minor phase whose space group is *P4/nmm*. The *P4/nmm* phase is ReAlSi, which has no Si/Al vacancies, and will be discussed in Chapter 4. The (200) peak of the as cast samples $ReAl_{0.3}Si_{1.525}$, $ReAl_{0.7}Si_{1.225}$, and ReAlSi were selected to highlight the gradual transition from predominantly the *X2/m(a0g)00* phase to the *P4/nmm* phase, shown in Figure 13. An overlay of all the Si-rich samples can be seen in Appendix B. Annealing caused the phases to segregate with a comparison between the AsCast and Annealed $ReAl_{0.3}Si_{1.525}$ samples shown in Figure 14.

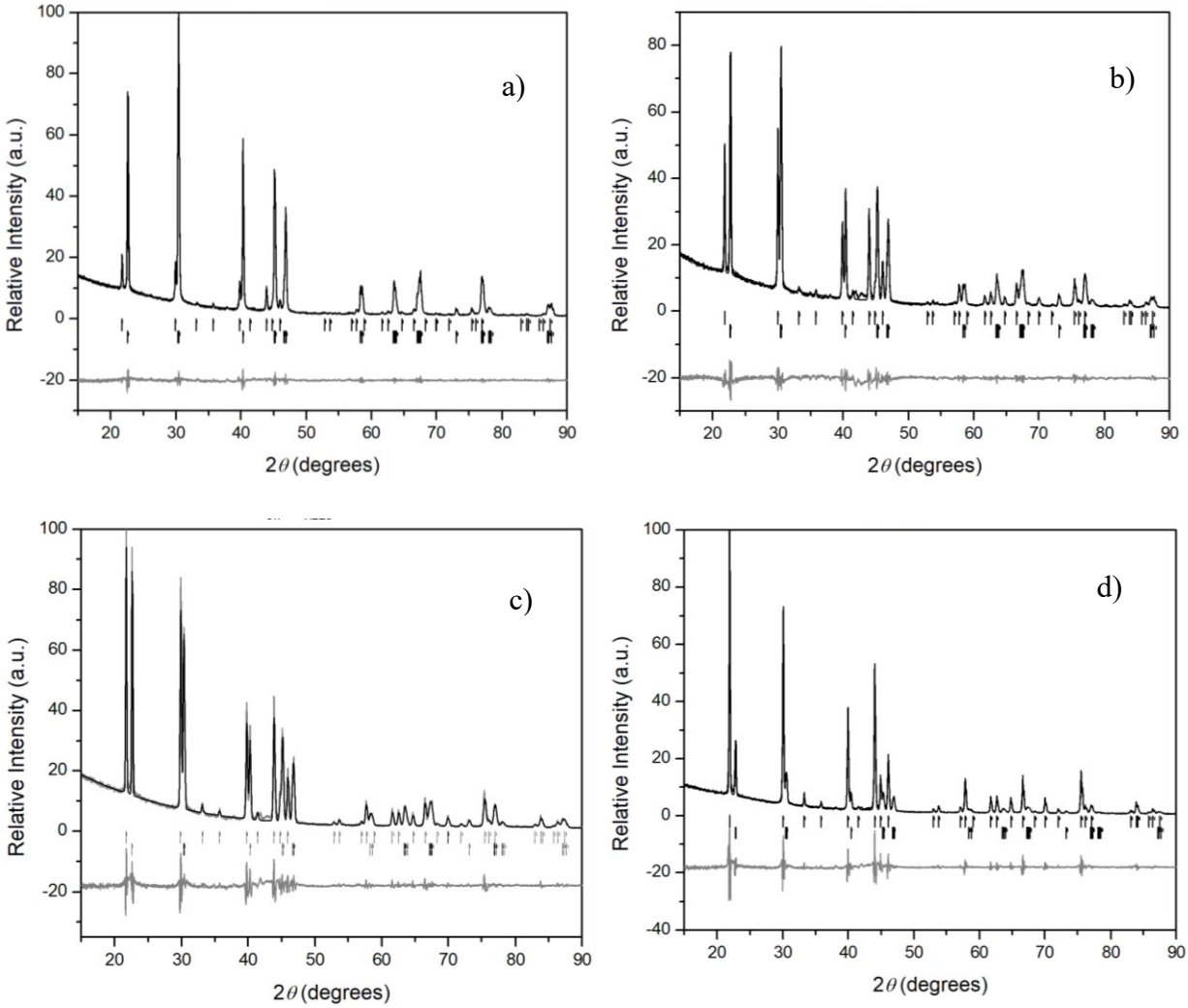

Figure 12. PXRD patterns of Si-rich series. PXRD patterns of a) $ReAl_{0.3}Si_{1.525}$ b) $ReAl_{0.5}Si_{1.375}$ c) $ReAl_{0.7}Si_{1.225}$ and d) $ReAl_{0.9}Si_{1.}075$. Upper vertical hashes represent the *P4/nmm* phase with the lower hashes depicting the *Immm* phase corresponding to the superspace group.

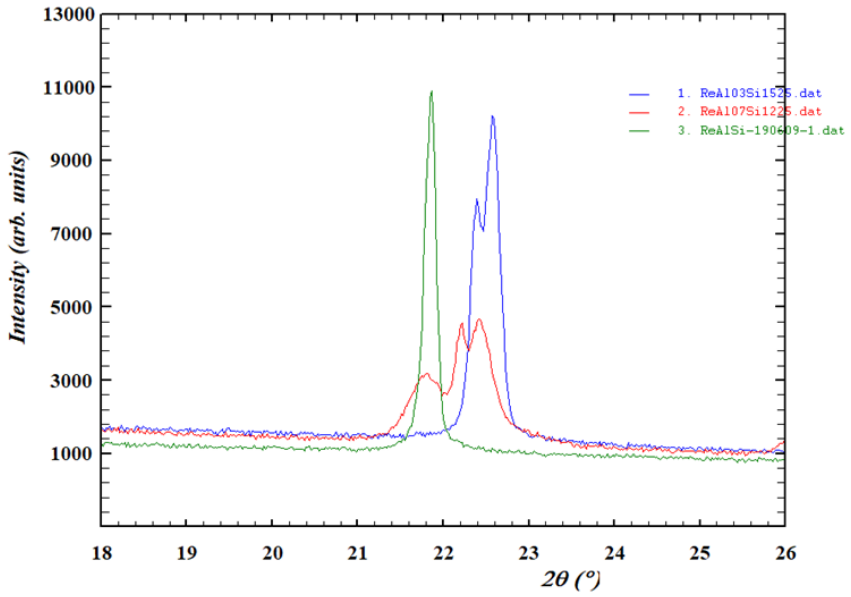

Figure 13. PXRD multiphase transition. Depicted are peaks corresponding to the (200) plane of three different powder samples. This comparison of peaks belonging to the same plane shows the samples were multiphase.

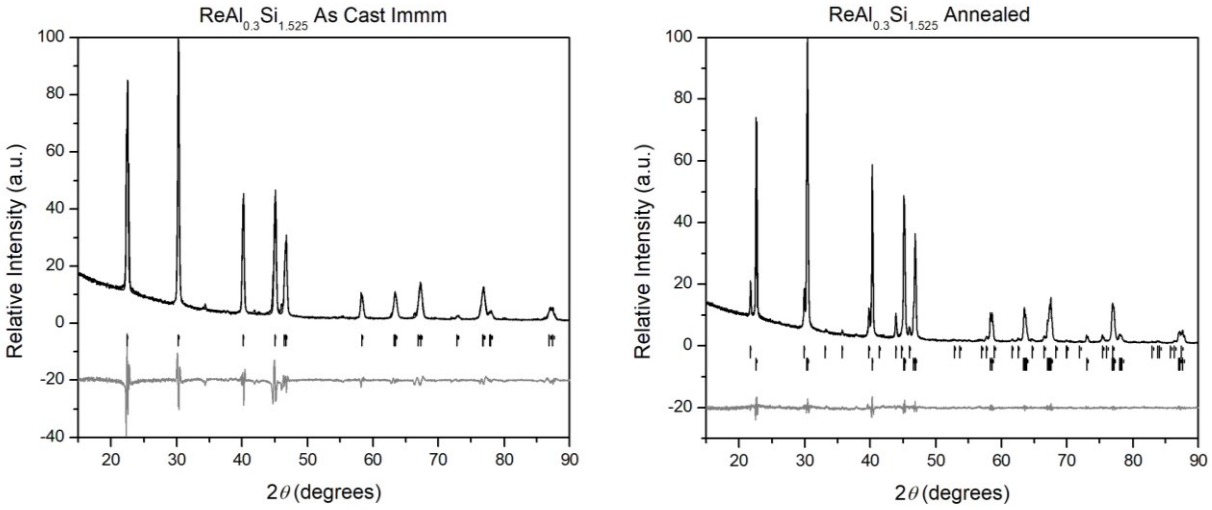

Figure 14. As Cast compared to annealed samples. Depicted are the PXRD patterns generated for the $ReAl_{0.3}Si_{1.525}$ samples. The pattern on the left depicts the As Cast sample, while the pattern on the right is from a sample which was annealed.

CHAPTER 4: ALUMINIUM-RICH RHENIUM-ALUMINIUM-SILICON TERNARY COMPOUNDS

4.1 Overview

Compositions studied from ReAlSi to $ReAl_2$ comprise the aluminium-rich series. The ratio of ReAlSi being 1:1:1 with (18 – 4) valence electrons per formula unit (f.u.), omits the need for vacancies and therefore was suspected to have a similar crystal structure to $MoSi_2$. ReAlSi was determined to be primitive instead of body-centered, thus differing from the $MoSi_2$ structure, and this difference was attributed to the segregation of Al and Si atoms, which was seen in previous research regarding the crystal structure of ReGaSi. [38] Therefore, crystallographic data was collected to determine if the crystal structure of $ReAl_{1.2}Si_{0.8}$ would be body-centered or primitive, and whether Al and Si atoms are segregated. Al-richer samples, such as $ReAl_{1.2}Si_{0.8}$, were synthesized to have less than (18 – 4) valence electrons. We tested these "electron-deficient" compositions to determine how strict the (18 – n) electron rule is. Previous research has also shown Al-Si and Re-Si binary compounds are superconducting and therefore superconductivity was determined for ternary rhenium aluminium silicide compounds. [32, 33, 25]

4.2 ReAlSi and $ReAl_{1.2}Si_{0.8}$

4.2.1 SXRD Data. SXRD diffraction patterns reveal that ReAlSi and $ReAl_{1.2}Si_{0.8}$ have an evident distinction – ReAlSi has a primitive unit cell, while $ReAl_{1.2}Si_{0.8}$ is body-centered. This is shown by comparing their reciprocal (1*kl*) planes in Figure 15. The odd ($h + l + k$) reflections are systematically absent in $ReAl_{1.2}Si_{0.8}$ but present in ReAlSi. The structural refinement of ReAlSi and $ReAl_{1.2}Si_{0.8}$ is provided in Table 4.

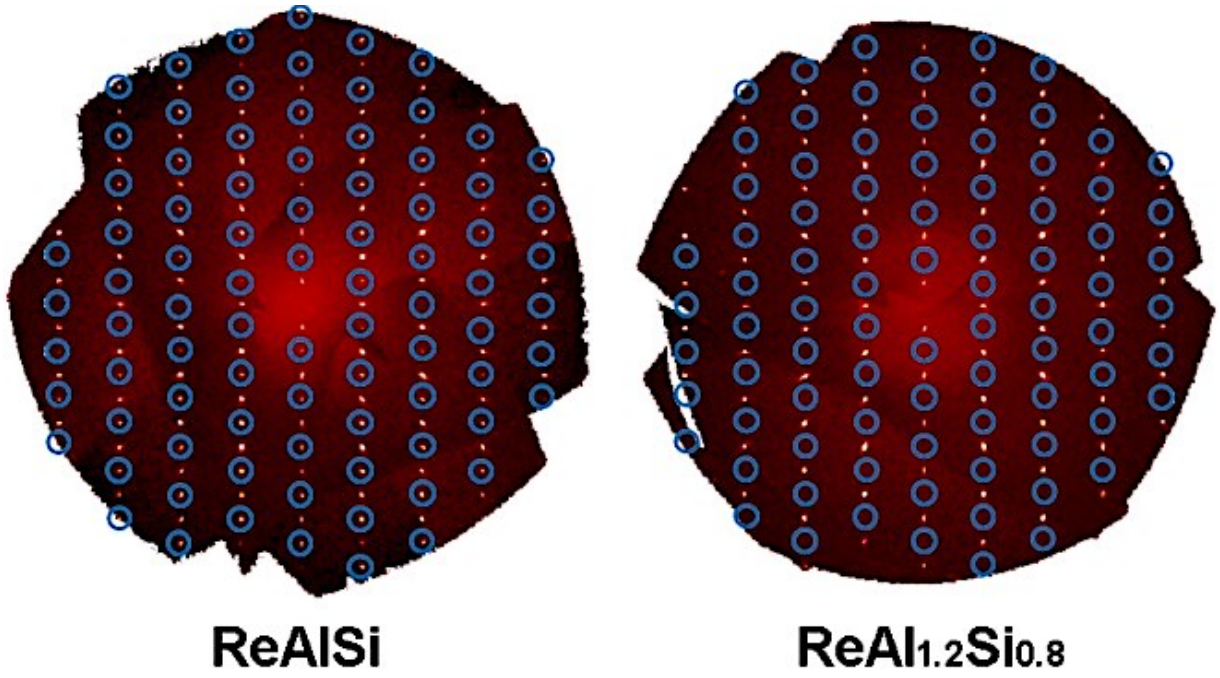

Figure 15. SXRD 1*kl* planes of ReAlSi and $ReAl_{1.2}Si_{0.8}$. The body-centering in $ReAl_{1.2}Si_{0.8}$ is shown through the systematic absence of odd ($h + l + k$) reflections (indicated by the blue circles). These reflections are present in ReAlSi, proving it is not body-centered.

The crystal structures of ReAlSi and $ReAl_{1.2}Si_{0.8}$ are shown and compared with ReGaSi and $MoSi_2$ in Figure 16. ReAlSi has a *P4/nmm* space group, just like ReGaSi,[38] and $ReAl_{1.2}Si_{0.8}$ is in *I4/mmm*, the same with $MoSi_2$. The difference between ReAlSi and $ReAl_{1.2}Si_{0.8}$ is thus the same as the difference between ReGaSi and $MoSi_2$ and can be demonstrated with the spacing between the (100) Re/Mo planes. The (100) Re/Mo planes of the $MoSi_2$ and $ReAl_{1.2}Si_{0.8}$ are evenly spaced by ½ of the *c*-axis, as opposed to the (100) Re planes of the ReGaSi and ReAlSi crystal structures, which are not evenly spaced (Figure 16). The subtle difference between ReAlSi and $ReAl_{1.2}Si_{0.8}$, we suspect, is that Al and Si are segregated in ReAlSi, just like how Ga and Si segregated in ReGaSi, but statistically mixed in $ReAl_{1.2}Si_{0.8}$. This is proven by neutron diffraction discussed below.

Table 4. SXRD data collection and refinement information for doping series.

Loading Composition	ReAlSi	$ReAl_{1.2}Si_{0.8}$
Crystal system, space group	Tetragonal, *P4/nmm*	Tetragonal, *I*4/*mmm*
Temperature (K)	293	293
a, b, *c* (Å)	3.1780 (6), 8.0372 (14)	3.195 (4), 8.092 (9)
V (Å^3)	81.17 (2)	82.63 (13)
Z	2	2
μ (mm^{-1})	75.49	74.12
Crystal size (mm)	0.07 × 0.06 × 0.05	0.08 × 0.07 × 0.07
No. of measured, independent and observed [$I > 3\sigma(I)$] reflections	1403, 119, 119	728, 63, 63
R_{int}	0.028	0.050
$(\sin\theta/\lambda)_{max}$ (Å^{-1})	0.765	0.764
$R[F^2 > 2\sigma(F^2)]$, $wR(F^2)$, S	0.016, 0.020, 1.59	0.016, 0.018, 1.50
No. of parameters	11	7
$\Delta\rho_{max}$, $\Delta\rho_{min}$ (e Å^{-3})	1.11, −3.63	1.17, −1.19

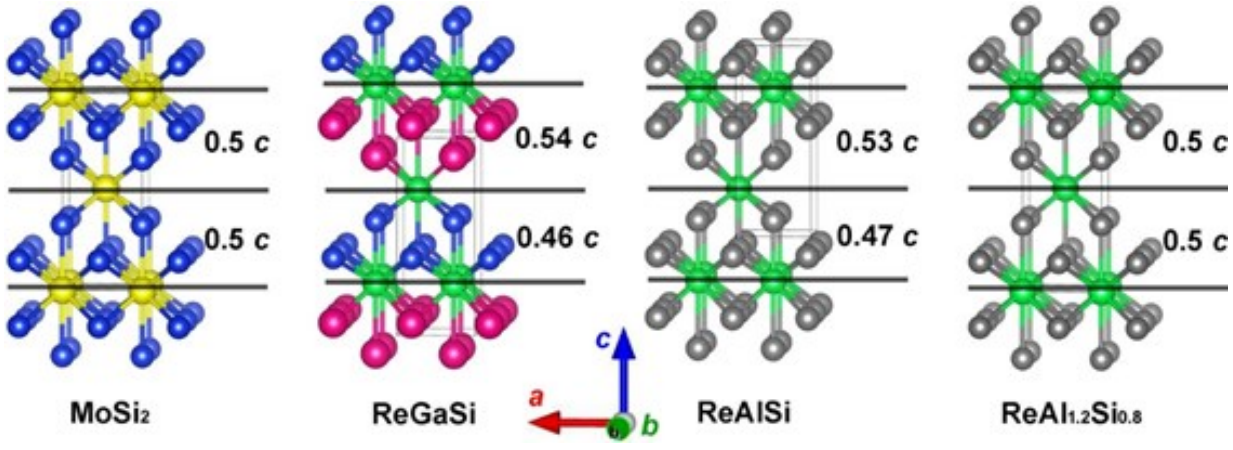

Figure 16. Crystal structures of $MoSi_2$, ReGaSi, ReAlSi, and $ReAl_{1.2}Si_{0.8}$. Color code: Mo, yellow; Si, blue; Re, green; Ga, red; Al/Si, grey.

4.2.2 PXRD Data. Powder diffraction of the as cast ReAlSi sample showed a, within reason, pure phase *P4/nmm* space group, but the annealed ReAlSi sample required two phase refinement suggesting an additional phase came out during annealing, a comparison can be seen in Figure 17. The main phase was the tetragonal *P4/nmm* space group, with a second minor phase refined with a body-centered *Immm* space group. This minor phase was determined to be either binary $ReSi_{1.75}$ or its Al-poor ternary variants, whose average structures are all in *Immm* space group (see Chapter 3). Annealing the ReAlSi sample caused the second phase (*Immm*) to become more apparent. The intensity of the peaks associated with the *P4/nmm* phase show this is the predominant phase. The odd ($h + k + l$) planes shown in the powder diffraction pattern of the ReAlSi samples, indicate the primitive unit cell. Structures obtained from SXRD were used to index and refine the diffraction patterns. Refinement of the Al-rich series was relatively simple, since each sample showed the SXRD predicted space group *I4/mmm*, with $ReAl_{1.2}Si_{0.8}$ refined in Figure 18.

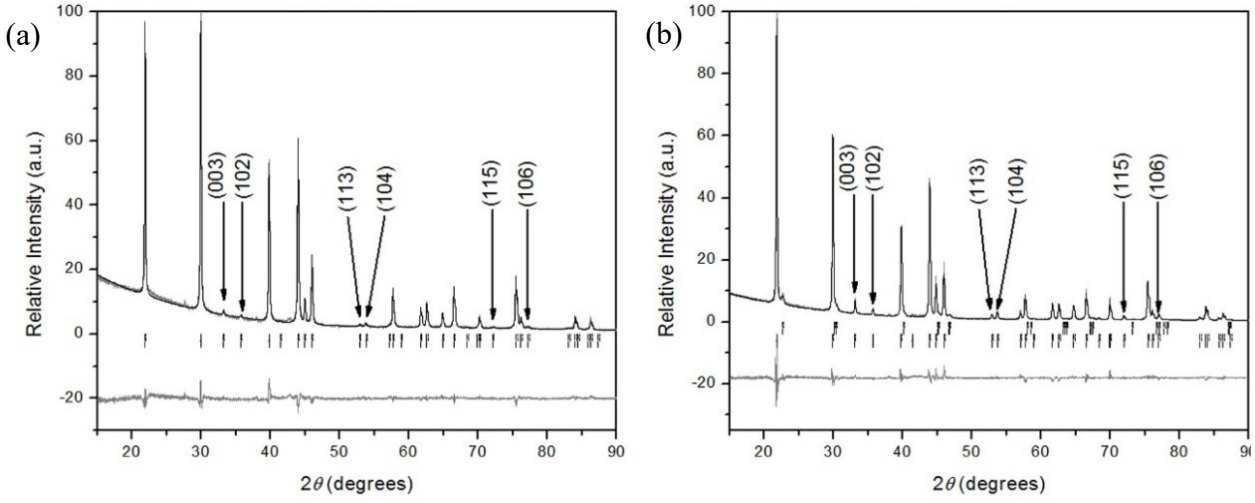

Figure 17. PXRD of ReAlSi as cast and annealed. (a) Depicts the as cast ReAlSi refined using the *P4/nmm* space group. (b) Shows the refinement for the annealed ReAlSi sample. This refinement required two-phases: *P4/nmm*, with peak positions shown using the lower vertical hashes; and *Immm*, with the upper vertical hashes showing the respective peak positions.

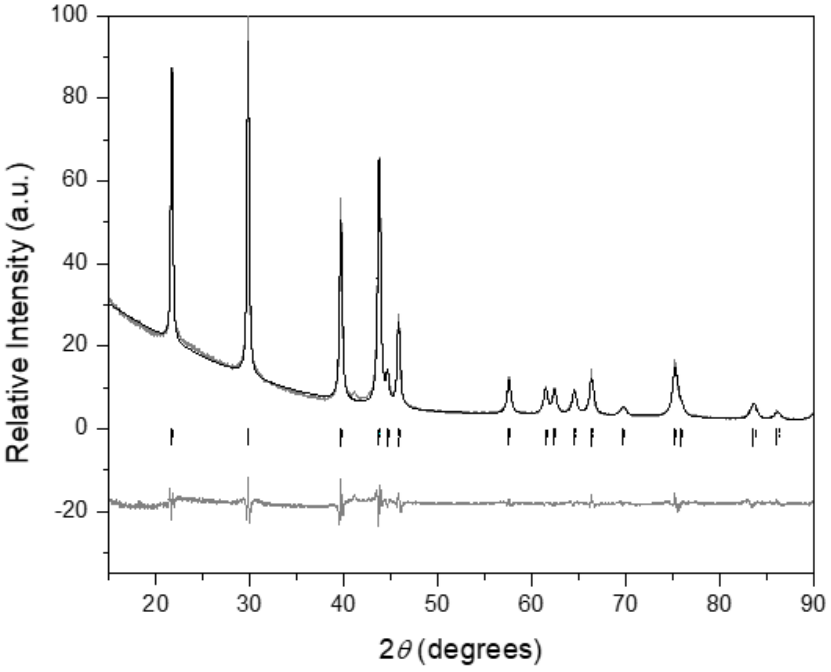

Figure 18. $ReAl_{1.2}Si_{0.8}$ annealed PXRD pattern. The vertical lines show the peak positions for the *I4/mmm* phase.

Table 5. PXRD refinement data for ReAlSi and $ReAl_{1.2}Si_{0.8}$.

Refined Composition	ReAlSi	$ReAl_{1.2}Si_{0.8}$
Crystal system, space group	Tetragonal, *P*4/*nmm*	Tetragonal, *I*4/*mmm*
Temperature (K)	293	293
a, *c* (Å)	3.1786, 8.0396	3.1803 8.0453
V (Å^3)	81.23	81.4
Z	2	2
R factors and goodness of fit	R_p = 0.0770, R_{wp} = 0.1067, R_{exp} = 0.0413, *R*(*F*) = 0.1102, χ^2 = 2.58	R_p = 0.0423, R_{wp} = 0.0552, R_{exp} = 0.0288, *R*(*F*) = 0.0240, χ^2 = 2.88
No. of data points	3824	3824
No. of parameters	11	12

4.2.3 Neutron Diffraction. Due to the limitations of PXRD and SXRD, neutron diffraction was necessary to differentiate between Al and Si atoms. It was hypothesized that Al and Si would segregate into separate layers in the ReAlSi sample, similar to the previously reported ReGaSi structure. [38] By comparison, since $ReAl_{1.2}Si_{0.8}$ is body-centered, Al and Si were expected to be statistically mixed. These speculations were confirmed through the Rietveld refinement of the neutron diffraction data, the patterns and refinement are shown in Figure 19. Refinement of the ReAlSi sample showed that Al and Si atoms occupy different 2*c* sites, while the $ReAl_{1.2}Si_{0.8}$ sample showed the Al and Si atoms shared the same 4*c* site with occupancies of 0.64 and 0.36 respectively, seen in Table 7. The site occupancy suggests a composition of $ReAl_{1.28(8)}Si_{0.72(8)}$, which is very close to the nominal loading composition, proving the accuracy of atom differentiation through neutron diffraction.

Table 6. Neutron diffraction data and Rietveld refinement for ReAlSi and $ReAl_{1.2}Si_{0.8}$ samples.

Refined Composition	ReAlSi	$ReAl_{1.28(8)}Si_{0.72(8)}$
Crystal system, space group	Tetragonal, *P*4/*nmm*	Tetragonal, *I*4/*mmm*
Temperature (K)	293	293
a, *c* (Å)	3.17757(8), 8.0370(3)	3.1815(1), 8.0447(4)
V (Å^3)	81.15(1)	81.43(1)
Z	2	2
R factors and goodness of fit	R_p = 0.052, R_{wp} = 0.070, R_{exp} = 0.032, $R(F)$ = 0.031, χ^2 = 4.973	R_p = 0.046, R_{wp} = 0.063, R_{exp} = 0.028, $R(F)$ = 0.021, χ^2 = 5.108
No. of data points	2000	2000
No. of parameters	24	24

Table 7. Neutron diffraction determination of atomic positions and isotropic atomic displacement parameters of ReAlSi and $ReAl_{1.2}Si_{0.8}$.

	ReAlSi					$ReAl_{1.28(8)}Si_{0.72(8)}$						
		x	y	z	U_{iso}*/U_{eq}			x	y	z	U_{iso}*/U_{eq}	Occ.
Re	2*c*	0	0.5	0.2661(2)	0.0036 (4)	Re	2*a*	0	0	0	0.0062(4)	1
Si	2*c*	0	0.5	0.5860(4)	0.0053 (7)	Si	4*e*	0	0	0.3373(3)	0.0056(6)	0.36(4)
Al	2*c*	0	0.5	−0.0871(5)	0.012 (1)	Al	4*e*	0	0	0.3373(3)	0.0056(6)	0.64(4)

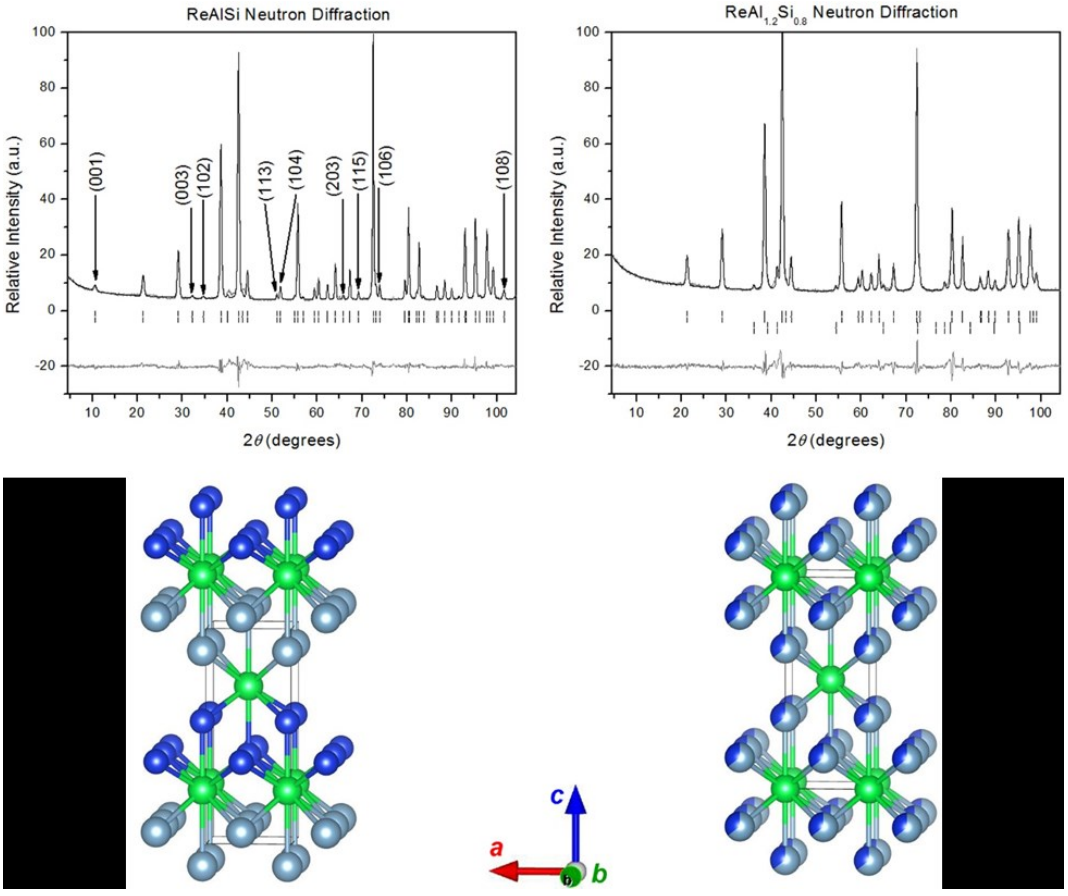

Figure 19. Neutron diffraction ReAlSi and $ReAl_{1.2}Si_{0.8}$ crystal structures. Color key: Re, green; Al, grey; Si, dark blue.

4.2.4 Computational Rationalization. Using VESTA, several models of crystal structures with the same compositions of ReAlSi and equal volume/f.u were built with different arrangements of Al and Si atoms. This was used to understand why the Al and Si atoms are segregated in the ReAlSi sample but statistically mixed in the $ReAl_{1.2}Si_{0.8}$ sample. Seventeen models were analyzed but the three most promising candidates are shown in Table 8; denoted as Model I, II and III. Model I was based on the experimentally determined structure for ReAlSi, with Al and Si atoms segregated into alternating layers between (001) Re planes. Models II and III varied the arrangement of Al and Si to compare the stability determined through first-principle calculations. The stability of the unit cells is quantified by the total energy (Etot), which is given in Table 8.

The integrated crystal Hamilton populations (ICOHP's) analyzed the bonding energy of Model I to understand why this model is the most stable. Negative values represent stronger bonding interactions, with the largest overall ICOHP belonging to Model I as shown in Table 6. The greatest contributor to the bonding strength of Model I was the bond between Re-Si atoms, with a value of -32.5852 eV/cell. So, Model I is more stable than Model II and III because it has the strongest overall bonding, which is attributed mainly to its strongest Re-Si bonding. More details of the computational study can be found in Alec Neeson's thesis.[39]

The reason why Model I has the strongest Re-Si bonding can be demonstrated in Figure 20. All three models have diagonal and vertical Re-Si bonds, but only Model I could strengthen (shorten) all the Re-Si bonds simultaneously. Models II and III are able to strengthen diagonal Re-Si bonds but in doing so the vertical Re-Si bonds lengthen and thus become weaker. Therefore, the segregation of Al and Si atoms maximizes Re-Si bonding and overall bonding resulting in the most stable configuration. $ReAl_{1.25}Si_{0.75}$ has less Si atoms than ReAlSi and

therefore has less Re-Si bonds. The limited number of Re-Si bonds in $ReAl_{1.25}Si_{0.75}$ limits the contribution of Re-Si bonding to the overall bonding and is no longer the main contributor. Therefore, configurational entropy takes precedence leading to a random distribution of Al and Si atoms as seen the neutron diffraction patterns.

Table 8. Computational model structures of ReAlSi.

Model	**Unit Cell**	**Relative E_{tot} (eV/cell)**	Re−Si ICOHP (eV/cell)	+	Re−Al ICOHP (eV/cell)	+	Al/Si−Al/Si ICOHP (eV/cell)	=	Total ICOHP (eV/cell)
I	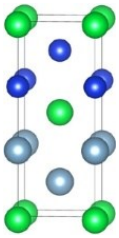	**0**	−32.5852		−24.1095		−14.3466		−71.0413
II	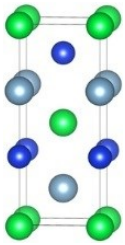	**0.0411**	−29.7964		−25.8734		−14.7226		−70.3924
III	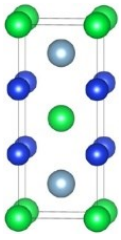	**0.3899**	−28.8688		−26.6500		−14.8960		−70.4148

The calculated relative total energy (Etot) and integrated crystal orbital Hamiltonian population (ICOHP) of the ReAlSi samples are provided below. Color key: Re, green; Al, grey; Si, dark blue. [39]

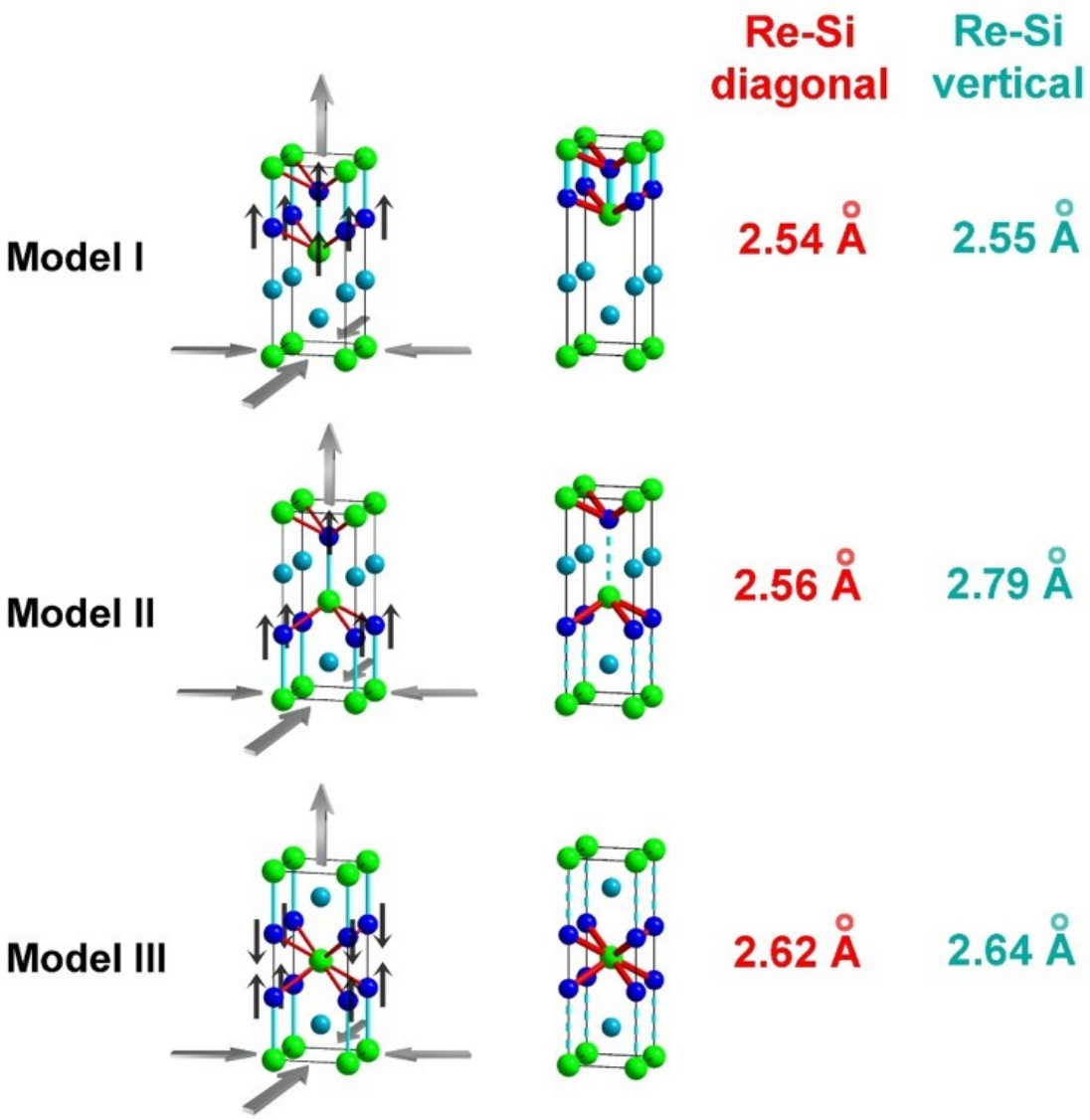

Figure 20. Computational ReAlSi model structures. Atom color code: Re, green; Si, dark blue; Al, light blue. Bond color code: diagonal Re−Si, red; vertical Re−Si, light blue. The gray arrows show the elongation of the unit cells and the black arrows show the vertical movements of the atoms, both of which can shorten and enhance the diagonal Re−Si bonds (red). [39]

4.2.5 Superconductivity Data. The electrical resistivity of ReAlSi and $ReAl_{1.2}Si_{0.8}$ samples analyzed from 5 K to 300 K, show the samples behave similarly but the resistivity is ten times higher for ReAlSi compared to $ReAl_{1.2}Si_{0.8}$. At low temperatures, both samples become superconductors, where the $ReAl_{1.2}Si_{0.8}$ sample shows two transition temperature ranges, while

ReAlSi has only one. The resistivity of $ReAl_{1.2}Si_{0.8}$ at ~4.7 K to 4.1 K reduces drastically from over 100 $\mu\Omega$-cm to 25 $\mu\Omega$-cm, and, after a narrow step, further drops to 0 at ~3.4 K, shown in Figure 21. The transition temperature of ReAlSi ranges from ~4.1 K to ~3.2K, where it exhibits zero-resistivity. This superconductive transition in ReAlSi is comparable to the second transition expressed by $ReAl_{1.2}Si_{0.8}$ in regard to the transition temperature range.

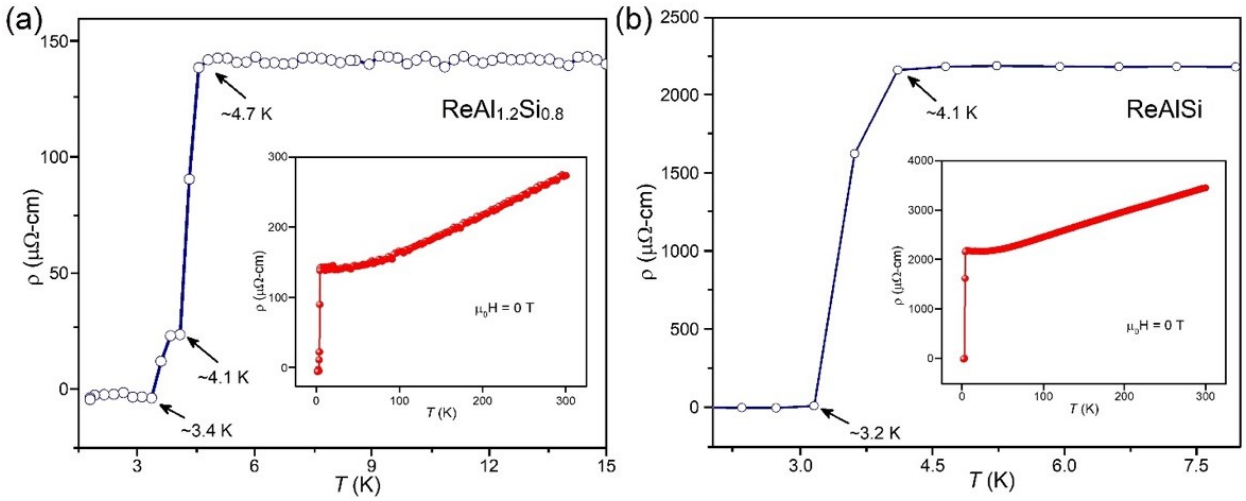

Figure 21. ReAlSi and $ReAl_{1.2}Si_{0.8}$ temperature dependent resistivities. a) The transition temperatures and corresponding resistivity for $ReAl_{1.2}Si_{0.8}$. b) The gradual transition temperature for ReAlSi, notice the tenfold resistivity values.

The temperature-dependence of resistivity under various magnetic fields (0 – 5 T) was measured for $ReAl_{1.2}Si_{0.8}$ from 1.8 K to 6 K, as seen in Figure 22. The temperature-dependence of resistivity under various magnetic fields shows the second superconductive transition starting at ~4.1 K becomes quenched in a magnetic field of 0.5 T, while the first superconductive transition starting at ~4.7 K does not quench until a strong magnetic field of 5 T is applied. From this information one can infer that the superconductivity at ~4.7 K is much stronger and has better diamagnetism than the superconductivity expressed at ~4.1 K.

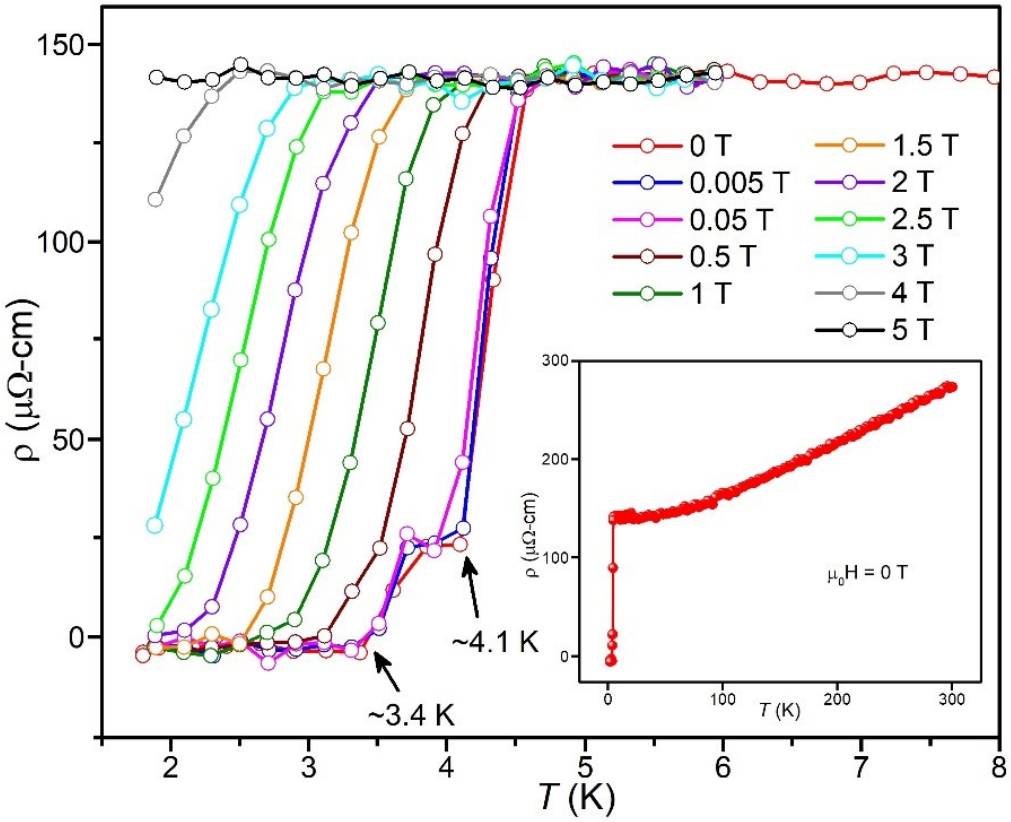

Figure 22. Temperature-dependent resistivity in external magnetic fields. This image shows how the superconductivity of $ReAl_{1.2}Si_{0.8}$ is affected by an applied external magnetic field. The smaller graph shows the resistivity of $ReAl_{1.2}Si_{0.8}$ from 1.8 K to 300 K, without an applied magnetic field.

The field-dependent resistivity at various temperatures (1.8 – 4.5 K) was also analyzed for $ReAl_{1.2}Si_{0.8}$ from 0 to 6 T, shown in Figure 23. In a strong magnetic field of 2 T, $ReAl_{1.2}Si_{0.8}$ still expresses superconductivity at 1.8 K, showing a strong magnetic field capability. Using the magnetic field-dependence and the relative temperatures at which the resistivity drops, we were able to use the Ginsberg-Landau relation to determine the upper critical field limit, and the critical temperature for the superconductivity expressed at ~4.7 K. The yielded T_c = 4.67(5) K and $\mu_0 H_{c2}$ (0) is 6.6(1) T, which is smaller than the Pauli limiting field for weak electron-phonon coupling (which tells the strength of the electron-phonon interaction) BCS superconductors 1.85

T_c, which for T_c = 4.67 K gives 8.6 T. The critical field of the lower-T_c transition (starting at ~4.1 K) is difficult to determine since it is suppressed with a magnetic field no larger than 0.5 T, which is totally overlapping with the higher-T_c transition.

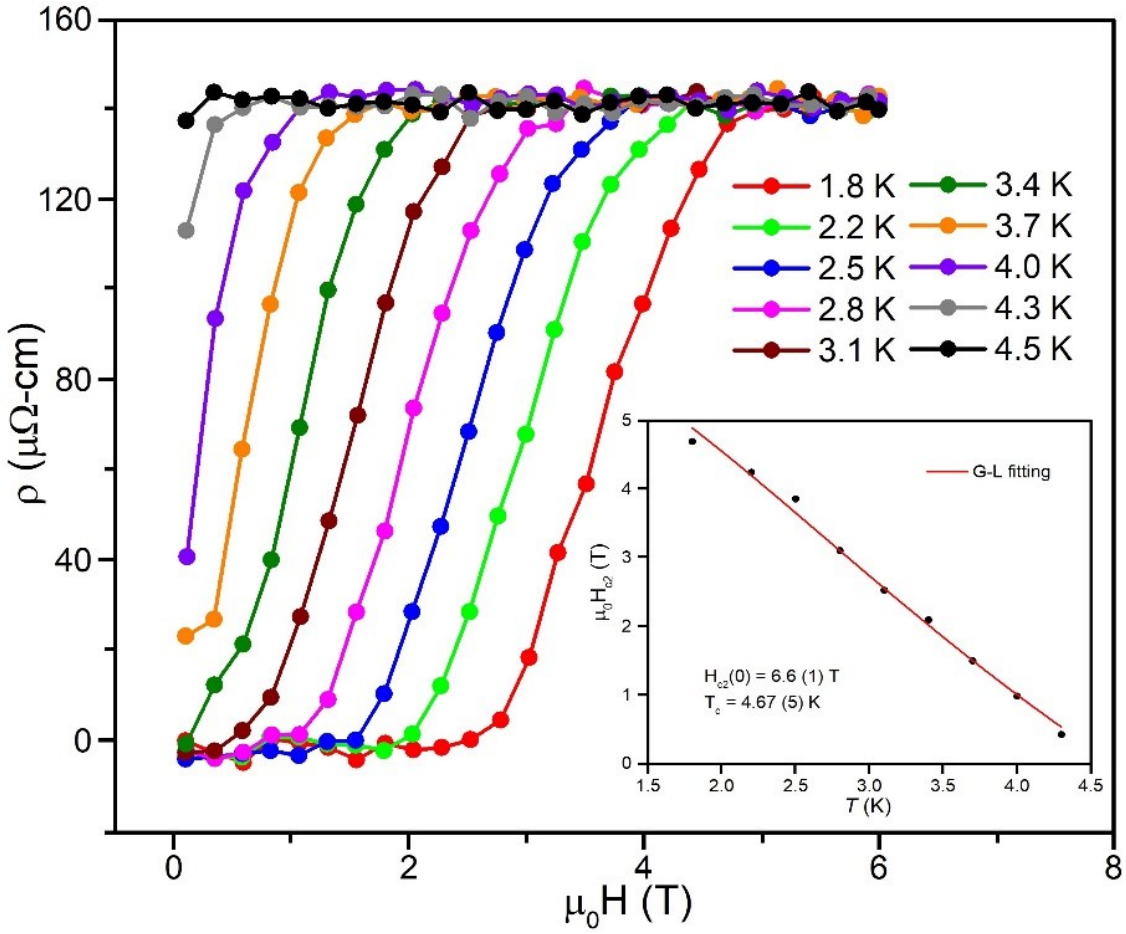

Figure 23. Field-dependent resistivity. The resistivity of $ReAl_{1.2}Si_{0.8}$ was analyzed in applied magnetic fields ranging from 0 T to 6 T under various temperatures from 1.8 K to 4.5 K. The internal graph shows the results for the Ginsberg-Landau relation, used to determine the upper critical field fitting.

4.2.6 Heat Capacity. Heat capacity measurements between 1.8 K to 300 K were taken for both $ReAl_{1.2}Si_{0.8}$ and ReAlSi in order to understand the similar resistivity transitions (starting at ~4.1 K) expressed by each sample shown in Figure 24. Heat capacity compares temperature dependence (Cp/T) vs T in order to relate the change in entropy ($\Delta S = \int_{T_1}^{T_2} \frac{C_p}{T} dT$) expressed by a

material as the material enters the phase transition of becoming superconductive. The C_p/T vs T for both ReAlSi and $ReAl_{1.2}Si_{0.8}$ above 4 K expressed no heat capacity jump, suggesting that the superconductive resistivity transition between 4.7 K and 4.1 K is not from the bulk but from superconductive impurities with a critical temperature of ~4.6 K. The impurity, which contributed to the superconductivity of $ReAl_{1.2}Si_{0.8}$, has yet to be determined and requires further investigation. Most probably, it is from a Re-Si solid solution with hexagonal close packing (*hcp*) structure, which was identified in the neutron diffraction pattern of $ReAl_{1.2}Si_{0.8}$. Previous reports have shown Re-Si solid solutions are superconducting and have T_c ranging from 1.7 to 5.2 K. [30] Figure 24 contains the heat capacity fitting results. Extrapolation gives $\gamma = 0.809(5)$ mJ/mol-K^2, and $\beta = 0.0329(1)$ mJ/mol-K^2 for ReAlSi, while $\gamma = 1.039(3)$ mJ/mol-K^2, and $\beta = 0.0409(1)$ mJ/mol-K^2 for $ReAl_{1.2}Si_{0.8}$. The heat capacity jump occurs at 3.5 K for both samples, indicating the same superconductive species present in both. The calculated superconductive parameter ($\Delta C/\gamma T_c$) was determined to be 0.21 for ReAlSi, and 0.94 for $ReAl_{1.2}Si_{0.8}$, both of which are lower than value of 1.43 predicted by BCS theory, indicating a 66 wt-% purity for $ReAl_{1.2}Si_{0.8}$ and 15 wt-% purity for ReAlSi. The impurity causing the heat capacity jump for ReAlSi is believed to be $ReAl_{1.2}Si_{0.8}$ since the superconductivity jumps for each sample are at a similar temperature of 3.5 K. This is reasonable because $ReAl_{1.2}Si_{0.8}$ and ReAlSi are so close in composition and their structures are both closely related to the $MoSi_2$-type, so it is very probable that one occurs as the minor phase during the synthesis of the other. The PXRD patterns of the ReAlSi sample (Figure 17) cannot provide explicit evidence that $ReAl_{1.2}Si_{0.8}$ exists because the peaks of the latter all coincide with the former. However, PXRD shows that the annealed ReAlSi sample harbors $ReSi_{1.75}$ (Si-richer) as a minor phase so, implicitly, there ought to be at least an Al-richer minor phase such as $ReAl_{1.2}Si_{0.8}$ to balance the composition.

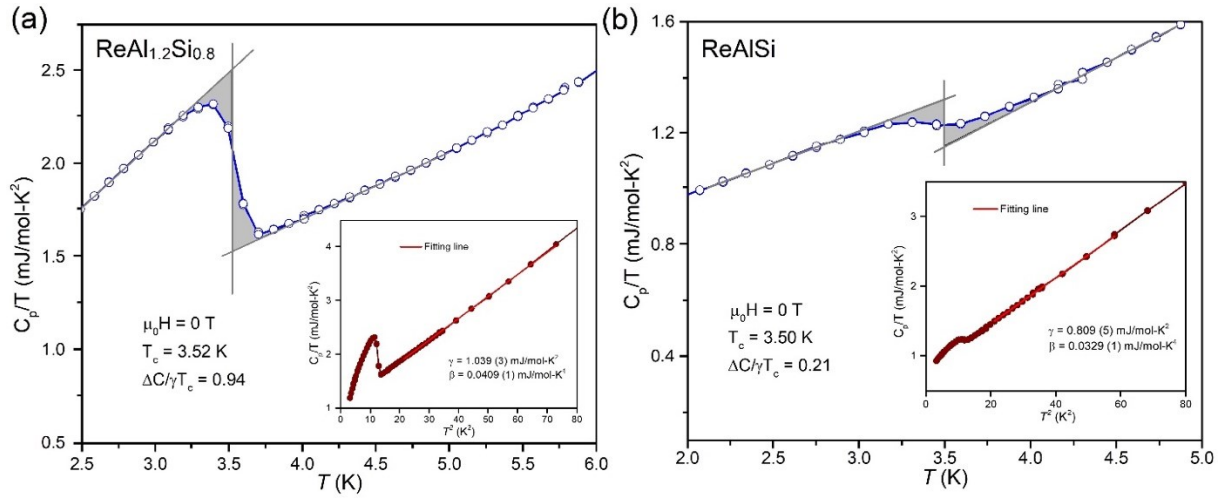

Figure 24. Temperature-dependence of C_p/T. These graphs show the low-temperature region of C_p/T vs T for (a) $ReAl_{1.2}Si_{0.8}$ and (b) ReAlSi; where the grey lines and shaded area represents the determination of $\Delta C/T_c$, and the internal graph shows the C_p/T vs T^2 where the red line indicates the heat capacity fitting.

4.2.7 Magnetic Properties. The temperature-dependence of volume magnetic susceptibility ($4\pi\chi_V$) for $ReAl_{1.2}Si_{0.8}$ was measure under a magnetic field of 0.005 T using both Zero Field Cooling (ZFC) and Field Cooling (FC), as shown in Figure 25. This figure describes the superconducting volume fraction of a sample. Volume magnetic susceptibility, from the ZFC method, reaches -1 at ~2 K suggesting almost all of the sample is under a superconducting diamagnetic state. This seems to be refuted by the heat capacity results which show $\Delta C/\gamma T_c$ = 0.94 , implying a 66 wt% purity, though this discrepancy could be due to a demagnetization effect or because the results depend on sample shape and orientation with respect to the direction of the external magnetic field. The ZFC also shows that the superconducting T_c at 4.7 must be due to impurities, since the ZFC curve starts to drop at around 3.5 K. The FC signal is considerably weaker, which is commonly seen in polycrystalline sample and may have been caused by strong flux trapping in our material.

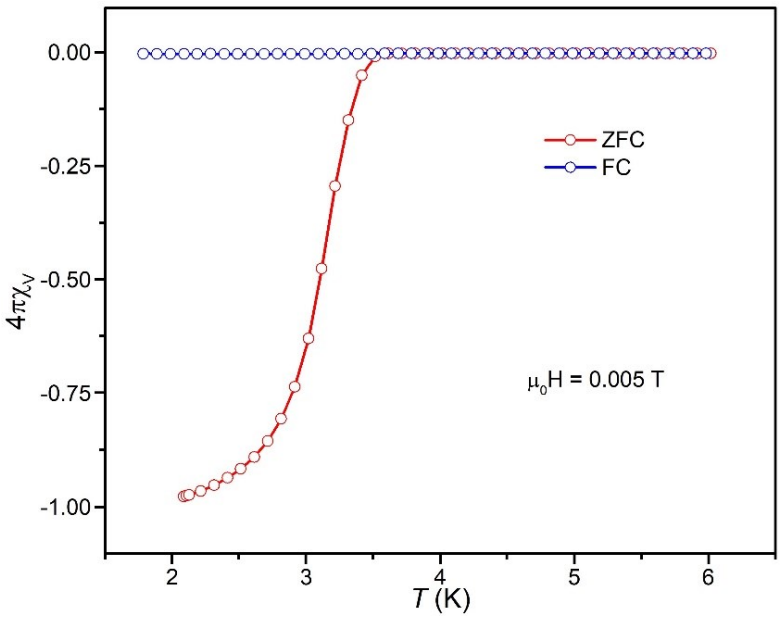

Figure 25. Temperature-dependence of volume magnetic susceptibility. Temperature dependence of volume magnetic susceptibility for $ReAl_{1.2}Si_{0.8}$ with ZFC (red) and FC (blue) methods under applied magnetic field of 0.005 T.

4.3 PXRD: $ReAl_{1.3}Si_{0.7}$ to $ReAl_2$

In order to determine the effects of defying the (18 – 4) electron rule, the Al-rich series increased the Al:Si ratio by 0.1 increments. As the Al-doping increases the electron count lowers. The crystal structure remained *I4/mmm* with a second phase appearing from leached rhenium atoms, which became more predominant as the electron count decreased, until $ReAl_{1.5}Si_{0.5}$ (Figure 26). $ReAl_{1.5}Si_{0.5}$ has an *I4/mmm* phase and a second unknown phase, which was not due to leached Re or Al atoms. At $ReAl_2$ the electron count is deficient an electron per f.u., which generated a diffraction pattern that was not able to be refined using an *I4/mmm* space group, the, possibly multiphase, structure remains unknown (Figure 27). The leaching of Re atoms can be attributed to the skewed electron count and would explain why more Re leached out of the crystal structure as the electron count became more deficient.

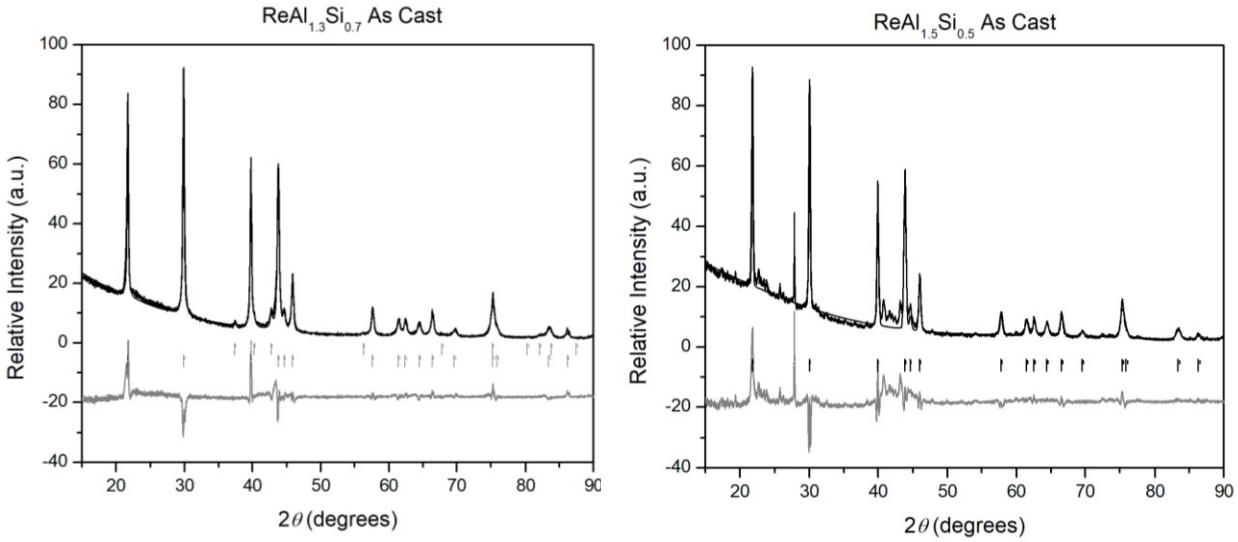

Figure 26. PXRD of $ReAl_{1.3}Si_{0.7}$ and $ReAl_{1.5}Si_{0.5}$. Lower hashes correspond to the *I4/mmm* phase, while the upper hash lines depict the leached rhenium atoms. $ReAl_{1.5}Si_{0.5}$ has only one set of hashes corresponding to the *I4/mmm* phase.

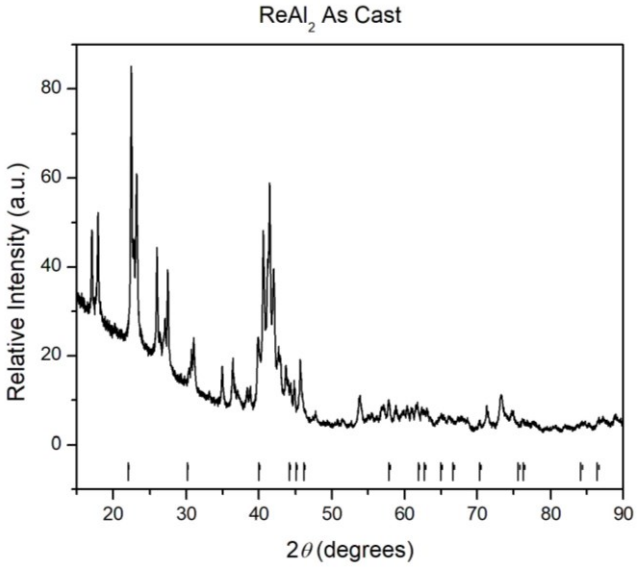

Figure 27. PXRD of $ReAl_2$. The lower hashes are used to show how the diffraction pattern strays from the *I4/mmm* space group. This pattern cannot be indexed with the *I4/mmm* space group at all.

CHAPTER 5: CONCLUSION

Previous research regarding transition-metal silicide's has shown doping improves some physical properties, while altering the crystal structure. Our research was an in-depth look into the crystal structures formed when rhenium silicide is doped with aluminium, and which physical properties were affected or expressed. This was accomplished by calculating the doping ratio using the (18-n) electron rule and then synthesizing the samples in a non-thermal plasma arc furnace. Each sample was analyzed using various crystallographic methods, then ReAlSi and $ReAl_{1.2}Si_{0.8}$ where analyzed through various methods to determine their superconductivity. As expected, our research showed that the crystal structure is altered through doping and continued to change as the doping ratio increased. We also discovered a new superconductive material $ReAl_{1.2}Si_{0.8}$, contributing to our hypothesis that the crystal structure affects physical properties. This contributes to findings made by the Eiji *et al*. group and Dr. Wang's previous research regarding the change from a *Cm* space group for binary rhenium silicide to an incommensurate superspace group *X2mm(α00)s0s* with the thermoelectric properties improving respectively.[25, 27]

Increasing the doping ratio of aluminium to silicon we saw the crystal structure changes from a $MoSi_2$-type structure for $ReSi_{1.75}$ with a commensurate **q** vector of (1/8, 0, 1/8) firstly to the superspace group *X2/m(α0γ)00* with an incommensurate **q** vector of (0.1106, 0, -0.0758) and then to another incommensurate structure with the superspace group Pm(α0γ)0 and **q** vector of (0.3266, 0, 0.1928) (Figure 11). These 2 new incommensurate phases need to be further studied for their physical properties such as thermoelectricity.

Increasing the amount of aluminium doping showed a second phase, *P4/nmm*, gradually increasing until it became the predominant phase at ReAlSi, as shown in the powder diffraction data (Figures 12 and 17). Neutron diffraction analysis showed that the aluminium and silicon

atoms were segregated in the ReAlSi sample (Figure 19). This segregation was explained using computation coloring, which showed that segregation was energetically more stable because it optimizes the Re-Si bonding, which is the strongest bonding in the structures (Table 8 and Figure 20). This primitive tetrahedral structure transitioned to a body-centered tetrahedral *I4/mmm* crystal structure with an increase in the doping ratio (Figure 15). The aluminium-rich samples had mixing of aluminium and silicon atoms, with a ratio of 0.64(4) and 0.36(4) respectively according to the neutron diffraction data, which was supported by the computational coloring due to less Re-Si bonding.

Physical property measurements were collected for ReAlSi and $ReAl_{1.2}Si_{0.8}$ because it was discovered, for the first time, that superconductivity was expressed for these samples. ReAlSi had a much greater electrical resistivity than $ReAl_{1.2}Si_{0.8}$ though both samples showed a superconductive transition at 4.1 K and expressed zero-resistivity at ~3.2 K. $ReAl_{1.2}Si_{0.8}$ had an addition T_c at 4.7 K (Figure 21). The temperature-dependent resistivity for $ReAl_{1.2}Si_{0.8}$ showed T_c at 4.1 K quenched in a 0.5 T external magnetic field, ten-fold less than the external magnetic field required to quench the 4.7 K superconducting transition (Figure 22). Field-dependence also showed a strong magnetic field capability with zero-resistance occurring at 1.8 K under a magnetic field of 2 T for $ReAl_{1.2}Si_{0.8}$ (Figure 23). The superconducting transition temperatures between 4.1 K and 4.7 K was determined to be caused by an unknown impurity (with a critical temperature of ~4.6 K, most likely, an *hcp*-structured Re-Si solid solution) due to the lack of an obvious heat capacity jump for both samples. An obvious jump did occur at 3.5 K for both species, though much larger for $ReAl_{1.2}Si_{0.8}$ (Figure 24). This jump is believed to be caused by $ReAl_{1.2}Si_{0.8}$ based on the mixing of Al and Si atoms, the crystal structure and varied electron

count. The Zero-Field-Cooling confirms that the transition at 4.7 K is due to impurity by maintaining a zero-volume magnetic susceptibility until 3.5 K (Figure 25).

Further research would be required to determine the unknown impurity contributing to the superconductive transition occurring at 4.7 K. Comparable data for the silicon-rich series, regarding conductive properties or lack thereof, would be desirable for an overall picture but due to time and resource constraint only ReAlSi and $ReAl_{1.2}Si_{0.8}$ were able to be analyzed. Synthesizing samples using an arc melt furnace has limitations to accuracy regarding doping ratios due to the occasional ejection of materials during melting caused by excessive energy and static electricity. The superspace group samples required use of another facility's single crystal diffractometer and therefore it was not possible to have all the silicon rich samples individually tested. While the respective powder diffraction patterns were able to be reasonably refined with the superspace group *X2/m(a0g)00*, it is possible that another superspace group would be a better fit or that the **q** vector would be changed.

REFERENCES

[1] V. Pecharsky, P. Zavalij, *Fundamentals of Powder Diffraction and Structural Characterization of Materials,* Springer US, **2009**, pp. 1-100.

[2] M. Ladd, *Crystal Structures: Lattices and Solids in Stereoview*, Horwood Publishing, **1999**, pp. 2-39.

[3] B. D. Cullity, *Elements of X-ray Diffraction*. 2nd ed. Addison-Wesley, **1978**.

[4] T.L. Brown, H.E. LeMay, B.E. Bursten, C.J. Murphy, *Chemistry: The Central Science*. Pearson/Custom Pub., **2013**, pp. 406-408.

[5] T. Fukuda, W. Menz, *Micro Mechanical Systems: Principles and Technology*; Elsevier: Amsterdam, **1998**, pp. 21-23.

[6] A. Authier, "The Reciprocal Lattice", can be found under https://www.iucr.org/education/pamphlets/4/full-text, **1981**.

[7] L. Ooi, *Principles of X-Ray Crystallography*, Oxford University Press, **2010**, pp. 28-30.

[8] A.M. Glazer, *A Journey Into Reciprocal Space: A Crystallographer's Perspective*, Morgan & Claypool Publishers, **2017**, pp. 3-27.

[9] J. Epp, *Materials Characterization Using Nondestructive Evaluation (NDE) Methods,* Woodhead Publishing, **2016**, pp. 81-124.

[10] K. Fucke, J. W. Steed, *Water.* **2010**, 2, 333–350.

[11] T. Janssen, B. McMahon, "Aperiodic Crystal", can be found under http://reference.iucr.org/dictionary/Aperiodic_crystal, **2017**.

[12] S.V. Smaalen, *Incommensurate Crystallography*, OUP Oxford, **2007,** pp. 5-26.

[13] T. Janssen, B. McMahon, "Superspace Group", can be found under https://dictionary.iucr.org/Superspace_group. **2017**.

[14] The Editors of Encyclopaedia Britannica, "Semiconductor", can be found under https://www.britannica.com/science/semiconductor **2019**.

[15] L. I. Berger, *Semiconductor Materials*, CRC Press, **1997**, pp. 18-28.

[16] B. Averill, P. Eldredge, *General Chemistry: Principles, Patterns, and Applications*, Flat World Knowledge, Inc., **2013**, pp. 1136-1141.

[17] D. T. Morelli, *Thermoelectric Materials*. Springer Cham, **2017**.

[18] Y. Pei, H. Wang, G. J. Snyder, *Ad. Mater.* **2012**, 24 (46), 6125–6135.

[19] D. M. Rowe, *CRC Handbook of Thermoelectrics*, CRC Press, **2018**, pp. 575-577.

[20] "U.S. Energy Use Rises to Highest Level Ever", can be found under https://www.llnl.gov/news/us-energy-use-rises-highest-level-ever

[21] H. Suhl, B. T. Matthias, L. R. Walker, *Phys. Rev.* **1959**, *3* (12), 552–554.

[22] D. M. Ginsberg, "Superconductivity" can be found at https://www.britannica.com/science/superconductivity, **2018**.

[23] T. Siegrist, F. Hulliger, G. Travaglini, *Journal of the Less Common Metals* **1983**, *92*, 119–129.

[24] A. Qiu, L. Zhang, A. Shan, J. Wu, *Phys. Rev. B.* **2008**, 77.

[25] E. Terada, M. W. Oh, D. M. Wee, H. Inui, *MRS Proceedings* **2005**, 842, S5.7.1-S5.7.6

[26] U. Gottlieb, B. Lambert-Andron, F. Nava, M. Affronte, O. Laborde, A. Rouault, R. Madar, *Journal of Applied Physics* **1995**, *78*, 3902–3907.

[27] S. Harada, H. Hoshikawa, K. Kuwabara, K. Tanaka, E. Okunishi, H. Inui, *Philosophical Magazine* **2011**, *91* (23), 3108–3127.

[28] F. Wang, I. Veremchuk, S. Lidin, *European Journal of Inorganic Chemistry*, **2017**, 47–55.

[29] J. Chevrier, D. Pavuna, F. Cyrot-Lackmann, *Physical Review B* **1987**, *36*, 9115–9121.

[30] J. L. Jorda, M. Ishikawa, J. Muller, *J. Less Common Met.* **1982,** *85,* 27 – 35.

[31] T. Siegrist, J. Greedan, J. Garrett, G. Wenhe, C. Stager, *Journal of the Less Common Metals* **1991**, *171*, 171–177.

[32] R. Dronskowski, S. Kikkawa, A. Stein, *Handbook of Solid-State Chemistry*, Wiley-VCH, **2017**, .

[33] V. J. Yannello, D. C. Fredrickson, *Inorganic Chemistry* **2014**, *53*, 10627–10631.

[34] V. J. Yannello, D. C. Fredrickson, *Inorganic Chemistry* **2015**, 54, 11385–11398.

[35] D. C. Fredrickson, M. Boström, Y. Grin, S. Lidin, *Chem. Euro. Journal* **2009**, 15 (33), 8108–8112.

[36] V. Petříček, M. Dušek, L. Palatinus, *Zeitschrift für Kristallographie - Crystalline Materials* **2014**, *229*.

[37] S. Steinberg, R. Dronskowski, *Crystals,* **2018**, 8 (5), 225.

[38] W. Xie, L. Gustin, G. Bian, *Inorganic Chemistry* **2017**, *56* (9), 5165–5172.

[39] A. Neeson, *Elucidation of an Anomalous Potential Thermoelectric Rhenium Silicon Aluminum Crystal*, thesis, **2020**.

APPENDICES

Appendix A

Figures of PXRD data for Si-rich series not included in the body of the thesis.

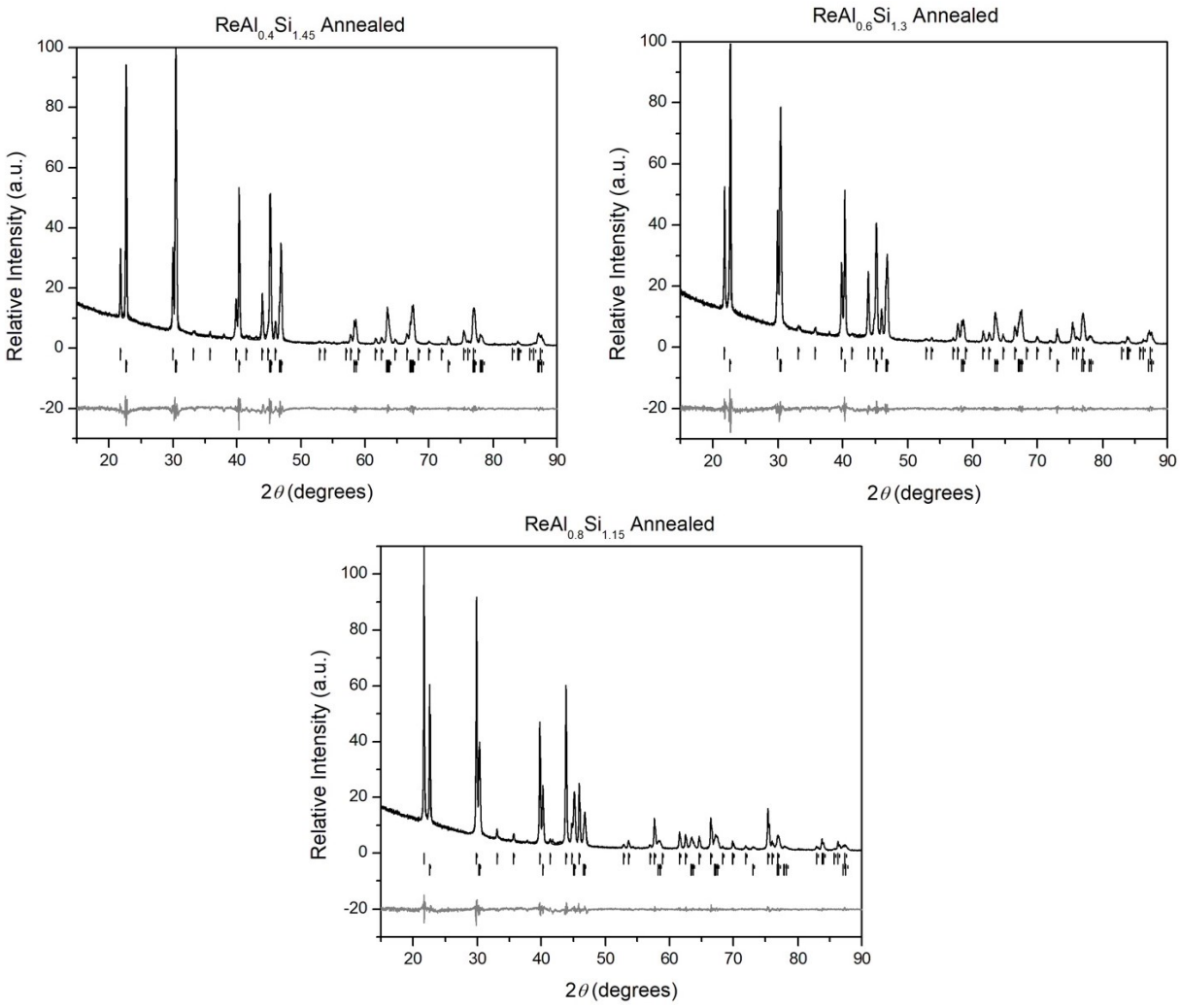

Appendix B

Figure of the (200) peak of the entire Si-rich series.